Instability driven by boundary inflow across shear: a way to circumvent Rayleigh's stability criterion in accretion disks?

R. R. Kerswell†

School of Mathematics, Bristol University, Bristol BS8 1TW, UK

We investigate the two-dimensional (2D) instability recently discussed by Gallet *et al.* (*Phys. Fluids*, vol. 22, 2010, 034105) and Ilin & Morgulis (*J. Fluid Mech.*, vol. 730, 2013, pp. 364–378) which arises when a radial cross-flow is imposed on a centrifugally stable swirling flow. By finding a simpler rectilinear example of the instability – a sheared half-plane, the minimal ingredients for the instability are identified and the destabilising/stabilising effect of inflow/outflow boundaries clarified. The instability – christened 'boundary inflow instability' here – is of critical layer type where this layer is either at the inflow wall and the growth rate is $O(\sqrt{\eta})$ (as found by Ilin & Morgulis (*J. Fluid Mech.*, vol. 730, 2013, pp. 364–378)), or in the interior of the flow and the growth rate is $O(\eta \log 1/\eta)$, where η measures the (small) inflow-to-tangential-flow ratio. The instability is robust to changes in the rotation profile, even to those which are very Rayleigh-stable, and the addition of further physics such as viscosity, three-dimensionality and compressibility, but is sensitive to the boundary condition imposed on the tangential velocity field at the inflow boundary. Providing the vorticity is not fixed at the inflow boundary, the instability seems generic and operates by the inflow advecting vorticity present at the boundary across the interior shear. Both the primary bifurcation to 2D states and secondary bifurcations to 3D states are found to be supercritical. Assuming an accretion flow driven by molecular viscosity only, so $\eta = O(Re^{-1})$, the instability is not immediately relevant for accretion disks since the critical threshold is $O(Re^{-2/3})$ and the inflow boundary conditions are more likely to be stress-free than non-slip. However, the analysis presented here does highlight the potential for mass entering a disk to disrupt the orbiting flow if this mass flux possesses vorticity.

Key words: general fluid mechanics, rotating flows, transition to turbulence

1. Introduction

Rotating flows are ubiquitous in nature and industrial applications, so understanding their stability continues to be an important and active area of research. The extent of this activity is perhaps best epitomised by the huge body of work studying Taylor–Couette flow (Couette 1888; Mallock 1888; Taylor 1923) – the flow between

† Email address for correspondence: R.R.Kerswell@bristol.ac.uk

two concentric cylinders rotating at different rates – which has become the laboratory paradigm of the subject (e.g. Fardin, Perge & Taberlet 2014; Tuckerman 2014 and references herein). Despite all this work, however, only very recently has it been realised that imposed radial flow can destabilise an otherwise stable rotating flow (Gallet, Doering & Spiegel 2010; Ilin & Morgulis 2013). The paper by Ilin & Morgulis (2013) is particularly revealing because it demonstrates that the (non-dimensionalised) flow

$$\boldsymbol{U}(r, \theta) = -\frac{\eta}{r}\hat{\boldsymbol{r}} + \frac{1}{r}\hat{\boldsymbol{\theta}} \qquad (1.1)$$

between two concentric cylinders at $r = 1$ and $r = a > 1$ is inviscidly unstable to infinitesimal two-dimensional (2D) oscillatory disturbances for either inflow $\eta > 0$ or outflow $\eta < 0$ providing η is not too large. This is surprising because, first, in the absence of radial flow, this rotating flow is (marginally) 'Rayleigh-stable', as the angular momentum of the flow nowhere decreases in magnitude radially (note this is strictly a condition on axisymmetric disturbances: Rayleigh (1917); Drazin & Reid (1981, §15.2)). Second, the flow also fails a requirement for 2D instability – the rotating flow version of Rayleigh's inflexion-point theorem (Rayleigh 1880: Drazin & Reid 1981, §15.3 and problem 3.2 p. 121). Third, it is also somewhat counterintuitive that the instability occurs for both converging and diverging radial flows, since the former are stable and the latter generally unstable when the rotation is absent, as in Jeffery–Hamel flow (e.g. Drazin 1999).

The results of Ilin & Morgulis (2013) also possess many intriguing features, of which four stand out. First, the existence of an imposed normal flow through the cylinder walls increases the order of the linear operator describing the evolution of small inviscid disturbances from the normal two to three. This means that an extra boundary condition has to be imposed beyond the usual no-normal-flow conditions at either cylinder wall. While it is straightforward to argue that this extra condition must be imposed at the inflow boundary (Ilin & Morgulis 2013), predicting the effect of a specific choice is less clear: if a no-slip condition is imposed there is instability, whereas a vanishing vorticity condition gives stability. Second, in the limit of vanishing radial flow ($\eta \to 0$), Ilin & Morgulis (2013) find growth rates which scale as $O(\sqrt{\eta})$ rather than the generic $O(\eta)$ one might expect. This unusual growth rate scaling arises because there are no discrete modes of the linear problem which can satisfy the usual two no-normal velocity conditions for $\eta = 0$. This gives rise to a non-standard singular perturbation analysis, the robustness of which is unclear to, say, changes in the rotation profile and/or to the addition of extra physics. Third, the $\eta \to 0$ asymptotics presented seems incomplete. The instability described in Ilin & Morgulis (2013) has a critical layer character, but only where this critical layer is actually at the inflow boundary. This suggests the existence of further instabilities with an interior critical layer separated from the boundary. Lastly, the mechanism for the instability is unclear. Cross-flow and shear would seem obvious ingredients, but rotation or curvature not necessarily so. It is also not apparent whether the energy to feed the instability comes wholly 'through the boundary' or is extracted at least in part from the (interior) rotational energy of the underlying flow.

To keep this study manageable, the focus here is on the $0 < \eta \ll 1$ situation, which represents small radial inflow on a predominantly rotating flow. The motivation for this (as in Gallet *et al.* 2010) is the accretion disk problem, where, certainly for cold and hence weakly ionised disks, the source of inferred disk turbulence remains a hotly

contested issue (e.g. Dubrulle *et al.* 2005; Shariff 2009; Balbus 2011; Ji & Balbus 2013). As a result there is considerable interest in uncovering robust linear instability mechanisms. Interestingly, the existence of the radial accretion flow is rarely included in theoretical models since it is so small – $O(1/Re)$ smaller than the azimuthal flow, where the Reynolds number Re is huge when based on a molecular viscosity (e.g. Dubrulle (1992) quote figures of 10^{14}–10^{26}) – and presumably its presence only felt over $O(Re)$ time scales which are far too large to be relevant (e.g. Shariff (2009) estimates that it would take longer than the age of the universe for molecular viscosity to diffuse momentum across a typical disk). However, the results of Ilin & Morgulis (2013) suggest that such a flow could actually drive linear instabilities over a much shorter $O(\sqrt{Re})$ time scale.

The plan of the paper is to start with perhaps the simplest example of the instability, which is just a sheared half-plane of fluid with imposed inflow. The effect of adding viscosity is discussed as well as the introduction of an outflow (suction) boundary so that the flow domain becomes a channel. Then the discussion turns to rotating flow with more general profiles, including the solidly Rayleigh-stable Keplerian profile $\boldsymbol{U} = 1/\sqrt{r}\hat{\boldsymbol{\theta}}$, to examine the robustness of the instability. The effect of further physics in the form of viscosity, three-dimensionality and compressibility are also broached. Finally, the nonlinear aspects of the instability are probed, ranging from a weakly nonlinear analysis around the primary 2D bifurcation through to secondary bifurcations and the ensuing fully 3D finite amplitude solutions.

The findings of the paper, organised under the various questions posed above, are as follows.

(1) *Is curvature or rotation important for the instability?* No, all the features of the instability are reproduced in a rectilinear flow with inflow described in § 2.1. The instability operates by advecting a source of vorticity at the inflow boundary across shear.

(2) *Are there other (non-boundary layer) modes of instability caused by an inflow boundary?* Yes, instabilities exist with interior critical layers distinct from the inflow boundary: see §§ 2.1.2 and 3.3 and expressions (2.12), (2.48) and (3.31). Their growth rates are $O(\eta \log(1/\eta))$, which, while much larger than $O(\eta)$, are smaller than the inviscid boundary layer modes found by Ilin & Morgulis (2013) and the equivalent viscous boundary layer modes found by Gallet *et al.* (2010).

(3) *Given the sensitivity to what is chosen for the extra boundary condition, how generic is the instability across possible boundary conditions?* For finite η the instability looks generic, with only a no-vorticity boundary condition obviously ensuring stability: see § 2.1. However, for $0 < \eta \ll 1$, any restriction on the normal derivative of the tangential velocity effectively kills the instability: see § 2.1.4. The non-slip condition always seems to allow instability to occur (Gallet *et al.* 2010; Ilin & Morgulis 2013).

(4) *How robust is the instability to different rotation profiles?* Very robust. The form of the shear is unimportant for the boundary layer instability and of secondary importance for the critical layer instability: see § 3.3.

(5) *What is the effect of adding viscosity?* The presence of viscosity introduces a threshold cross-flow of $O(Re^{-1})$ in the rectilinear situation where long streamwise wavelengths are permissible (Nicoud & Angilella 1997 and § 2.2) or $O(Re^{-2/3})$ for the rotational situation where the azimuthal wavenumber is an integer (Gallet *et al.* 2010 and § 3.4).

(6) *What is the effect of adding three-dimensionality?* Squire's theorem effectively holds for the boundary layer instabilities since only the shear at the boundary is important and curvature is secondary. As a result, adding three-dimensionality leads to less unstable disturbances: see § 5.

(7) *How robust is the instability to adding further physics?* The instability survives the addition of compressibility (see § 4), three-dimensionality (see § 5) and viscosity (see §§ 2.2 and 3.4). It is also insensitive to the exact shear present as long as it is non-vanishing (see § 3.3).

(8) *Has this instability been seen before* Gallet *et al.* (2010) *and* Ilin & Morgulis (2013)? Yes, in a rectilinear form by Nicoud & Angilella (1997), who studied 'generalised plane Couette flow' where a streamwise pressure gradient is imposed to counterbalance the effects of cross-flow in the streamwise momentum balance (see § 2). Doering, Spiegel & Worthing (2000) also saw the instability without an imposed pressure gradient. In this case the introduction of cross-flow not only adds a new flow component to the base state but also changes its cross-stream shear. From a stability perspective, how these two effects interact can be subtle, and 'suction' (as it is typically called) can be found to stabilise or destabilise existing shear instabilities (e.g. Hains 1971; Fransson & Alfredsson 2003; Guha & Frigaard 2010; Deguchi, Matsubara & Nagata 2014). The situation is similar in the Taylor–Couette problem, where radial flow can either stabilise or destabilise the well-known Taylor vortex instability (Chang & Sartory 1967; Bahl 1970; Min & Lueptow 1994; Kolyshkin & Vaillancourt 1997; Kolesov & Shapakidze 1999; Serre, Sprague & Lueptow 2008; Martinand, Serre & Lueptow 2009). The importance of the work of Gallet *et al.* (2010) and Ilin & Morgulis (2013) is that they studied the effect of radial flow on centrifugally stable Taylor–Couette flow.

(9) *Is the instability supercritical or subcritical?* It is a supercritical instability for bifurcations where the cross-flow is fixed and non-slip boundary conditions are applied at the boundaries in the presence of viscosity: see § 6.1 and appendix B.

(10) *Can secondary bifurcations off the 2D solutions reach cross-flow values which are below the threshold for (primary) instability?* There is no evidence for this. The six 3D bifurcations found are all supercritical, leading to even higher cross-flow values.

(11) *What is the energy source for the inviscid instability?* The instability draws its energy from the underlying shear. The energy of this is replenished by the pressure field, which drives the cross-flow, doing work.

(12) *Is this instability possibly relevant for accretion disks?* In a quiescent disk, the (molecular) viscosity-driven accretion flow is $O(Re^{-1})$, whereas the critical threshold for linear instability is a radial flow of $O(Re^{-2/3})$, leaving aside any issues about the exact form of the outermost boundary conditions. This, together with the fact that no signs of subcriticality have been found in either the primary instability or of any secondary bifurcations, indicates that the instability is not operative in isolation. However, if some other process is able to generate a larger radial flow, then this instability may be triggered as a secondary consequence. The instability primarily derives its energy from the gravitational body force working on the accreting flow.

Ilin and Morgulis have themselves continued their investigation to consider the effect of viscosity (Ilin & Morgulis 2015*a*) and three-dimensionality (Ilin & Morgulis 2015*b*), albeit from a complementary perspective: given a cross-flow what is the

smallest critical swirling flow for instability? This is equivalent upon rescaling to the problem of fixing the swirling flow and finding when instability disappears as the cross-flow is increased rather than decreased, as studied here. That there is a finite range of cross-flow for instability when there is both an inflow and outflow boundary appears a generic observation. There is also a tempting general interpretation – the inflow boundary is responsible for initially destabilising the flow as the cross-flow is increased in magnitude from zero, but ultimately the outflow (or more commonly labelled the 'suction') boundary stabilises the flow again when the cross-flow becomes large enough. The particularly simple half-plane problem treated below helps motivate this simple characterisation. We henceforth refer to the instability first seen by Nicoud & Angilella (1997), Doering *et al.* (2000), Gallet *et al.* (2010) and Ilin & Morgulis (2013) as the 'boundary inflow instability'.

2. 2D instability in simplest form: the half-plane

The boundary inflow instability operates by advecting vorticity across shear, occurs in 2D and does not need viscosity or underlying vorticity, as shown in Ilin & Morgulis (2013). Here, we demonstrate that curvature or rotation are not necessary either, by discussing a rectilinear example of the instability. The instability does need a boundary, however, so cannot be captured by a local analysis. To see this, consider the simplest possible set-up: a 2D shear flow

$$\boldsymbol{U} = y\hat{\boldsymbol{x}} + \eta\hat{\boldsymbol{y}}, \tag{2.1}$$

where there is a constant pressure gradient $-\eta\hat{\boldsymbol{x}}$ and $\boldsymbol{U}$ conveniently solves both the Euler equations and the Navier–Stokes equations by design (removing the pressure gradient means that the base state is no longer a constant shear in the viscous situation). The linearised inviscid equation for the perturbation vorticity $\omega = -\Delta\psi$, where ψ is the stream function ($\boldsymbol{u} = \nabla \times \psi\hat{\boldsymbol{z}}$), is

$$\left(\frac{\partial}{\partial t} + y\frac{\partial}{\partial x} + \eta\frac{\partial}{\partial y}\right)\omega = 0, \tag{2.2}$$

which represents just advection of the vorticity and has solution

$$\omega(x, y, t) = \omega_0(x - yt + \tfrac{1}{2}\eta t^2, y - \eta t), \tag{2.3}$$

where $\omega_0(x, y)$ is the initial vorticity distribution. In an unbounded domain, ω_0 can be Fourier transformed, so that it is sufficient to consider only $\omega_0 = \exp(i(kx + ly))$. Then the stream function is

$$\psi(x, y, t) = \frac{k^2 + l^2}{k^2 + (l - kt)^2}e^{i(kx + (l-kt)y + \eta[kt^2/2 - lt])}, \tag{2.4}$$

which exhibits transient growth but no linear instability, just as in the $\eta = 0$ case (Orr 1907; Farrell 1987).

2.1. *Half-plane: inviscid*

A half-plane, however, can permit a starting vorticity distribution which spatially grows towards the boundary. Consider a boundary at $y = 0$ and $\eta > 0$ so that this is an inflow boundary when the fluid domain is $y > 0$. Taking the Fourier transform

in x of (2.3) forces

$$\Delta\psi(x, y, t) = f(y - \eta t)\mathrm{e}^{\mathrm{i}k(x-yt+\eta t^2/2)}, \tag{2.5}$$

where f is an arbitrary function. If ψ is to be a modal disturbance which depends exponentially on t (and x), i.e. $\psi(x, y, t) = \hat{\psi}_k(y)\exp(\mathrm{i}kx + \sigma t)$, then

$$f(\xi) = A\mathrm{e}^{-(\sigma\xi + \mathrm{i}k\xi^2/2)/\eta} \tag{2.6}$$

is the only possibility (A is an arbitrary normalisation) and therefore

$$\left(\frac{\mathrm{d}^2}{\mathrm{d}y^2} - k^2\right)\hat{\psi}_k(y) = A\mathrm{e}^{-(\sigma y + \mathrm{i}ky^2/2)/\eta} \tag{2.7}$$

(no modal solution exists for $\eta = 0$). We will show that this equation, where the initial vortical distribution decays exponentially as $y \to \infty$, has growing modal disturbances (i.e. $\mathrm{Re}(\sigma) > 0$). No instability is possible if the boundary is an outflow boundary – i.e. $\eta < 0$ – as A is forced to be zero by boundedness. This suggests that the instability exists providing the boundary is not a zero-vorticity boundary which would force $A = 0$. In what follows, we adopt a non-slip boundary condition, as Ilin & Morgulis (2013) originally did, but will revisit this issue in §2.1.4 ((2.7) is a third-order differential equation for ψ, integrated once to include an arbitrary constant – hence three boundary conditions are needed to specify a unique solution).

  To confirm there is instability, (2.7) must be solved to derive the dispersion relation. Using a Green's function approach, setting A to 1 (w.l.o.g.) and imposing the two (usual inviscid) boundary conditions that $\hat{\psi}_k(0) = 0$ and $\lim_{y\to\infty}\hat{\psi}_k(y) = 0$, (2.7) has the solution

$$\hat{\psi}_k(y) = -\int_0^y \frac{\mathrm{e}^{-ky}}{k}\sinh(k\bar{y})\mathrm{e}^{-(\sigma\bar{y}+\mathrm{i}k\bar{y}^2/2)/\eta}\,\mathrm{d}\bar{y} - \int_y^\infty \frac{\mathrm{e}^{-k\bar{y}}}{k}\sinh(ky)\mathrm{e}^{-(\sigma\bar{y}+\mathrm{i}k\bar{y}^2/2)/\eta}\,\mathrm{d}\bar{y}. \tag{2.8}$$

A third boundary condition needs to be applied to give the dispersion relation and, with no-slip at the influx boundary ($\mathrm{d}\hat{\psi}_k/\mathrm{d}y = 0$ at $y = 0$), this is the relation

$$\int_0^\infty \mathrm{e}^{-k\bar{y}-(\sigma\bar{y}+\mathrm{i}k\bar{y}^2/2)/\eta}\,\mathrm{d}\bar{y} = 0. \tag{2.9}$$

There is no solution to this for $k = 0$, indicating the absence of a 1D instability, but there is instability in 2D ($k \neq 0$). The expression (2.9) is valid for finite η, but it is now useful to consider small η, where this instability can be understood as a critical layer instability. The (special) case where this critical layer is at the (influx) boundary (so it is in fact a boundary layer) was discussed by Ilin & Morgulis (2013) in their inviscid Taylor–Couette set-up. The growth rates for such modes are $\mathrm{Re}(\sigma) = O(\sqrt{\eta})$. The other (generic) case when the critical layer is distinct from the inflow boundary has not been discussed before. The growth rate here is smaller – $\mathrm{Re}(\sigma) = O(\eta\log(1/\eta))$ (see below) – but is still larger than the default $O(\eta)$ which would be expected.

  The asymptotic form of the dispersion relation (2.9) can be derived as $\eta \to 0^+$ using standard steepest descent/saddle point ideas. Here we need two parts of the integrand to contribute at the same leading order and precisely cancel. This can happen in two ways, since there is just one saddle point at $\bar{y}_s = \mathrm{i}\sigma/k$: the contribution from an end

point (clearly $\bar{y} = 0$) cancels the contribution from the saddle point (the interior critical layer case) or the saddle point and the end point are effectively one and the same asymptotically (the boundary layer case). In the former case, the leading contributions from the end point at $\bar{y} = 0$ (first term on the left-hand side in (2.10)) and from the saddle point (second term on the left-hand side) must satisfy

$$\frac{\eta}{\sigma} + \sqrt{\frac{2\pi\eta}{ik}}e^{-i\sigma - i\sigma^2/(2k\eta)} = 0. \tag{2.10}$$

Now, for the saddle point to be asymptotically separated from the endpoint $\bar{y} = 0$, $|\sigma/k| = O(1)$. This, together with the fact that the magnitude of the saddle point contribution $O(\sqrt{\eta}\exp(\sigma_r\sigma_i/(k\eta)))$ (where $\sigma = \sigma_r + i\sigma_i$) has to be $O(\eta)$ requires either $\sigma_r = O(1)$ and then $\sigma_i \ll 1$, or $\sigma_r \ll 1$ and $\sigma_i = O(1)$. The former case is inconsistent because the saddle point is in the wrong part of the $\bar{y}$-complex plane, leaving the contribution from the end point $\bar{y} = 0$ unbalanced. The latter situation, however, does yield solutions. Defining

$$\sigma = i\sigma_i + \delta(\eta)\tilde{\sigma}_r, \tag{2.11}$$

with σ_i and $\tilde{\sigma}_r$ both $O(1)$ quantities and $\delta(\eta) \to 0$ as $\eta \to 0$, then (2.10) requires

$$\delta(\eta)\tilde{\sigma}_r = -\frac{k\eta}{2\sigma_i}\left(\log\frac{1}{\eta} + \log\frac{2\pi\sigma_i^2}{k}\right) - k\eta + O(\eta^2\log 1/\eta), \tag{2.12}$$

and

$$\mathrm{Arg}[e^{i(\sigma_i^2/(2k\eta)+\pi/4)}] = O(\eta\log 1/\eta), \tag{2.13}$$

so there is instability with asymptotic growth rate $O(\eta\log 1/\eta)$ for a discrete set of frequencies

$$\sigma_i = -\sqrt{\tfrac{1}{2}\pi k\eta(8n-1)}, \tag{2.14}$$

where n is an integer of $O(1/\eta)$. The form of the corresponding eigenfunction is discussed in § 2.1.2.

The other situation – the boundary layer case – arises when the saddle point is within $O(\sqrt{\eta})$ of the endpoint at $\bar{y} = 0$, i.e. $|\sigma| = O(\sqrt{\eta})$. At this point, the endpoint and the saddle point contributions cannot be considered separately. Instead $\bar{y}$ and σ must be rescaled so that (2.9) becomes

$$\int_0^\infty e^{-\hat{\sigma}z - iz^2}\,dz = 0, \tag{2.15}$$

where $z := \bar{y}/\sqrt{2\eta/k}$ and

$$\sigma = \sqrt{k\eta/2}\,(\hat{\sigma}_r + i\hat{\sigma}_i) + O(\eta). \tag{2.16}$$

This must be solved numerically, but a good estimate for the eigenvalues can be found by treating the contributions from the end point and saddle point as if they are separated. This means taking the integer n to be $1 \ll n \ll 1/\eta$ in the frequency expression (2.14) for the internal critical layer mode and calculating the corresponding growth using (2.12). This leads to the asymptotic form

$$\hat{\sigma}_i \sim -\sqrt{\pi(8n-1)} \quad \hat{\sigma}_r \sim \frac{1}{|\hat{\sigma}_i|}\log(\pi\hat{\sigma}_i^2) \quad \text{as integer } n \to \infty, \tag{2.17a,b}$$

which performs very well even for the first eigenvalue since $\hat{\sigma}_i$ is already < -4.7 then: see table 1. Figure 1 shows a typical critical layer eigenfunction and three boundary layer eigenfunctions for $k = 1$ and $\eta = 10^{-3}$.
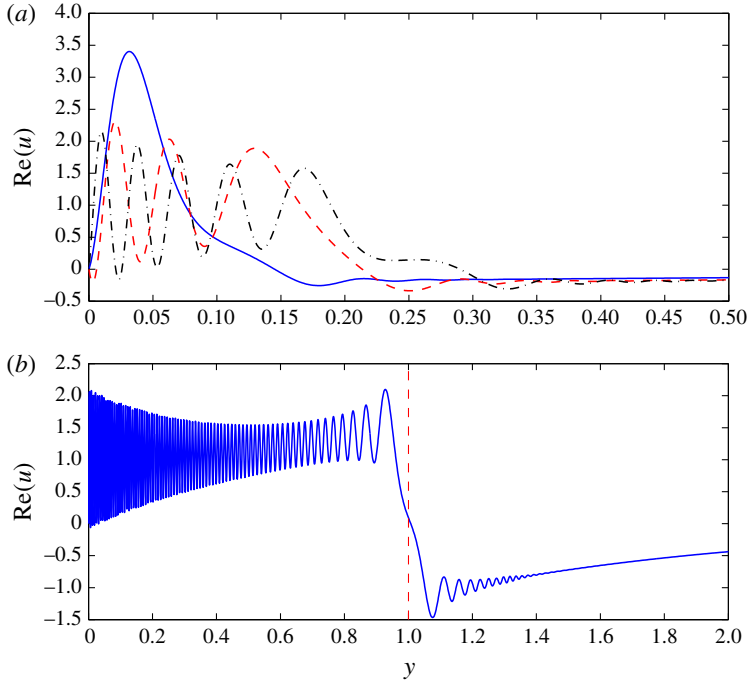
FIGURE 1. (Colour online) Unstable boundary layer eigenfunctions ((a): blue solid line is the most unstable, the red dashed line is the third most unstable and the black dash-dot line is the fifth most unstable mode) and an unstable critical layer eigenfunction ((b) with the critical layer shown as a red dashed line) for $\eta = 10^{-3}$ and $k = 1$. In all, the real part of $u = \psi_y$ is shown.

| | Asymptotic | | Actual | |
n	$\hat{\sigma}_i$	$\hat{\sigma}_r$	$\hat{\sigma}_i$	$\hat{\sigma}_r$
100	-50.1012	0.17909	-50.10143	0.1790934
10	-15.7539	0.42268	-15.75720	0.4226325
9	-14.9387	0.43871	-14.93867	0.4386500
8	-14.0684	0.45724	-14.07266	0.4571595
7	-13.1449	0.47903	-13.14981	0.4789312
6	-12.1513	0.50526	-12.15722	0.5051295
5	-11.0690	0.53781	-11.07620	0.5376254
4	-9.8686	0.57997	-9.877886	0.5796846
3	-8.5004	0.63820	-8.513168	0.6377301
2	-6.8647	0.72800	-6.884666	0.7270530
1	-4.6894	0.90317	-4.732350	0.9003686

TABLE 1. The 10 most unstable eigenvalues from the dispersion relation (2.15) and asymptotic estimates from (2.17).

2.1.1. *Inviscid asymptotics* $0 < \eta \ll 1$ *for the boundary layer instability*

Here a modal stream function solution of the form $\Psi(x, y, t) = \psi(y)e^{ikx+\sigma t}$ is sought with a boundary layer of thickness $\sqrt{\eta}$, as first uncovered by Ilin & Morgulis

(2013) (see their §3.2). Defining the new boundary layer variable $\xi := y\sqrt{k/(2\eta)}$ and splitting the stream function into an expansion of large-scale parts and a boundary layer corrections (hatted variables)

$$\psi := (\psi_0(y) + \hat{\psi}_0(\xi)) + \sqrt{\eta}(\psi_1(y) + \hat{\psi}_1(\xi)) + \cdots, \tag{2.18}$$

we look for an instability with vanishing frequency ($=k \times$ speed of the inflow boundary) to leading order,

$$\sigma := \sqrt{\eta k/2}\,\hat{\sigma} + O(\eta). \tag{2.19}$$

The governing equation

$$(\sigma + iky + \eta\partial_y)(\psi_{yy} - k^2\psi) = 0 \tag{2.20}$$

is then simplified to

$$\psi_{0yy} - k^2\psi_0 = 0 \tag{2.21}$$

for the leading flow and

$$(\hat{\sigma} + 2i\xi + \partial_\xi)\hat{\psi}_{0\xi\xi} = 0 \tag{2.22}$$

for its boundary layer correction. The interesting observation here is that there is no large-scale solution ψ_0 which can handle both the $\eta = 0$ boundary conditions that $v(x, 0, t) = 0$ and $\lim_{y\to\infty} v(x, y, t) = 0$. Crucially, this means that the boundary layer correction $\hat{\psi}_0$ must be $O(1)$ so as to contribute at leading order to fix up the $v(x, 0, t) = 0$ boundary condition, rather than the usual $O(\sqrt{\eta})$ to satisfy the extra $\eta \neq 0$ tangential boundary condition $u(x, 0, t) = 0$. As a consequence, there is an $O(1/\sqrt{\eta})$ tangential velocity u in the boundary layer which must vanish at $\xi = 0$. Since the large-scale flow cannot contribute at this order, this non-slip condition is solely on the boundary layer flow and is sufficient to determine the growth rate. Integrating (2.22) twice and incorporating the fact that $\lim_{\xi\to\infty} \hat{\psi}_{0\xi} = 0$, leads to

$$\hat{\psi}_{0\xi} = -A \int_\xi^\infty e^{-\hat{\sigma}z - iz^2}\,dz, \tag{2.23}$$

where A is an arbitrary constant. Imposing $u = 0$ at $y = 0$ then forces $\hat{\psi}_{0\xi}(0) = 0$, which is precisely condition (2.15).

2.1.2. *Inviscid asymptotics* $0 < \eta \ll 1$ *for the critical layer instability*

An interior critical layer instability is constructed by looking for a mode of $O(1)$ frequency. Adopting the expansion (2.11), where again both σ_i and $\tilde{\sigma}_r$ are $O(1)$, the critical layer is centred on $y_c := -\sigma_i/k$ (so $\sigma_i < 0$) and, as in the boundary layer case, has thickness $O(\sqrt{\eta})$. Defining the critical layer variable

$$\xi := \frac{y - y_c}{\sqrt{\eta}} \tag{2.24}$$

the (leading order) stream function in the critical layer, $\hat{\psi}$, satisfies

$$(\delta\tilde{\sigma}_r/\sqrt{\eta} + ik\xi + \partial_\xi)\hat{\psi}_{\xi\xi} = 0, \tag{2.25}$$

which can be integrated once to give

$$\hat{\psi}_{\xi\xi} = \sqrt{\eta}\, e^{-\delta\tilde{\sigma}_r\xi/\sqrt{\eta}-ik\xi^2/2} \tag{2.26}$$

(choosing the normalisation of the mode here for convenience later) and then two further times to give

$$\hat{\psi}_\xi = \sqrt{\eta}\left(\int_0^\xi e^{-\delta\tilde{\sigma}_r x/\sqrt{\eta}-ikx^2/2}\,dx + A\right) \sim \sqrt{\eta}\left(\pm\sqrt{\frac{\pi}{2ik}}+A\right) + \text{h.o.t.} \quad \text{as } \xi \to \pm\infty \tag{2.27}$$

$$\hat{\psi} = \sqrt{\eta}\left(\int_0^\xi (\xi - x)e^{-\delta\tilde{\sigma}_r x/\sqrt{\eta}-ikx^2/2}\,dx + A\xi\right) + B$$

$$\sim \sqrt{\eta}\xi\left[\pm\sqrt{\frac{\pi}{2ik}}+A\right] + B + \text{h.o.t.} \quad \text{as } \xi \to \pm\infty, \tag{2.28}$$

where A and B are $O(1)$ constants.

Outside the critical layer, the stream function consists of a WKB-type solution and simple exponentials which satisfy Laplace's equation,

$$y_c < y: \quad \psi_+ = C_+ e^{-ky} + \frac{E_+}{k^2(y-y_c)^2}e^{-[\delta\tilde{\sigma}_r(y-y_c)+ik(y-y_c)^2/2]/\eta} \tag{2.29}$$

$$0 < y < y_c: \quad \psi_- = C_- e^{-ky} + D_- e^{ky} + \frac{E_-}{k^2(y-y_c)^2}e^{-[\delta\tilde{\sigma}_r(y-y_c)+ik(y-y_c)^2/2]/\eta}, \tag{2.30}$$

where $C_\pm$, D_- and $E_\pm$ are constants whose order of magnitude will be set by matching to the critical layer stream function. The fact that ψ_+ and $d\psi_+/dy$ must vanish as $y \to \infty$ is imposed by including only the decaying exponential for $y > y_c$: the WKB mode vanishes as $y \to \infty$ when $\eta > 0$ provided $\tilde{\sigma}_r > 0$.

The governing equation (2.20) is third order and so ψ, ψ_y and ψ_{yy} must be continuous everywhere. The oscillatory form of $\hat{\psi}_{\xi\xi}$ in the critical layer means it must match entirely to the outer WKB-type solution

$$\psi^{WKB} := \frac{-\eta^{3/2}}{k^2(y-y_c)^2}e^{-[\delta\tilde{\sigma}_r(y-y_c)+ik(y-y_c)^2/2]/\eta} \tag{2.31}$$

either side of the critical layer so $E_\pm = -\eta^{3/2}$. This means that the outer WKB solution only contributes at $O(\sqrt{\eta})$ to the tangential velocity u near the critical layer, whereas the critical layer stream function $\hat{\psi}$ forces an $O(1)$ tangential flow (see (2.27)). As a result there must be a large-scale flow of $O(1)$ in both u and v outside the critical layer: this explains the scaling of the integration constants in (2.28) and means that $C_\pm$ and D_- are all $O(1)$. There are then six (complex) conditions to be satisfied at leading order by the five remaining constants and complex eigenvalue σ. The first four are matching conditions on u (ψ_y) and v ($-ik\psi$) as $y \to y_c^+$,

$$-kC_+ e^{-ky_c} = \sqrt{\frac{\pi}{2ik}}+A \quad \text{and} \quad C_+ e^{-ky_c} = B, \tag{2.32a,b}$$

and $y \to y_c^-$,

$$-kC_- e^{-ky_c} + kD_- e^{ky_c} = -\sqrt{\frac{\pi}{2ik}}+A \quad \text{and} \quad C_- e^{-ky_c} + D_- e^{ky_c} = B, \tag{2.33a,b}$$

or, eliminating A and B, simply two jump conditions across the critical layer

$$[u]_-^+ = \sqrt{\frac{2\pi}{ik}} \quad \text{and} \quad [v]_-^+ = 0. \tag{2.34a,b}$$

The two remaining (boundary) conditions, $v(x, 0, t) = 0$ and $u(x, 0, t) = 0$, require

$$C_- + D_- = 0 \quad \text{and} \quad -kC_- + kD_- - \frac{i\sqrt{\eta}}{ky_c}e^{[\delta\tilde{\sigma}_r y_c - iky_c^2/2]/\eta} = 0, \tag{2.35a,b}$$

where, while the outer WKB-type solution contributes at $O(\sqrt{\eta})$ to u near the critical layer, it must contribute at $O(1)$ to u at the inflow boundary. The resulting dispersion relation is

$$\frac{i\sqrt{\eta}}{ky_c}e^{[\delta\tilde{\sigma}y_c - iky_c^2/2]/\eta} + \sqrt{\frac{2\pi}{ik}}e^{-ky_c} = 0, \tag{2.36}$$

which leads to the same leading expressions for $\tilde{\sigma}_r$ and σ_i given in (2.12) and (2.14). The necessary change in the scaling of the WKB solution contribution gives the dominant $O(\eta \log 1/\eta)$ contribution to $\tilde{\sigma}_r$ and the exact numerical counterbalancing of the large-scale tangential flow gives the subdominant $O(\eta)$ contribution.

2.1.3. *The need for shear and inflow*

To emphasise that shear is a key ingredient of the instability, the above problem can be solved for the shearless flow $\boldsymbol{U} = \hat{\boldsymbol{x}} + \eta\hat{\boldsymbol{y}}$, leading to the requirement that there must exist $\text{Re}(\sigma) > 0$ with

$$\int_0^\infty e^{-k\bar{y} - \sigma\bar{y}/\eta} \, d\bar{y} = 0, \tag{2.37}$$

which is never satisfied. The presence of an inflow boundary is also crucial: converting the above inflow boundary to an outflow boundary ($\eta \to -\eta$) removes the instability. This is why the instability discussed here is not relevant to the considerable literature on suction boundary layers, where suction is always a stabilising effect (e.g. Joslin 1998).

2.1.4. *The third boundary condition*

Imposing the parametrised boundary condition $(1 - \beta)u + \beta \, du/dy = 0$ as the second boundary condition at $y = 0$ gives the modified dispersion relation

$$\int_0^\infty e^{-k\bar{y} - (\sigma\bar{y} + iky^2/2)/\eta} \, d\bar{y} = \frac{\beta}{1 - \beta} \tag{2.38}$$

($\beta = 0$ recovers non-slip and $\beta = 1$ a no-vorticity or equivalently stress-free condition as $v = 0$ along $y = 0$). For the boundary layer instabilities, the left-hand side is $O(\sqrt{\eta})$, so this dispersion relation can only be assumed similar to the non-slip relation (2.15) if $\beta \ll \sqrt{\eta}$. In fact, numerical computations indicate that the boundary layer instability is suppressed by $\beta \approx 2.6\sqrt{\eta/k} \ll 1$. For the critical layer instabilities, the condition (2.10) becomes a possible balance between three different terms

$$\frac{\eta}{\sigma} + \sqrt{\frac{2\pi\eta}{ik}}e^{-i\sigma - i\sigma^2/(2k\eta)} = \frac{\beta}{1 - \beta}, \tag{2.39}$$

where σ now has an $O(1)$ frequency as in (2.11). If $\beta \gg \eta$, the dominant balance is between the second and third terms (as opposed to the first and second for non-slip) and now leads to damped eigenvalues. It is then clear that, for instability to occur, there should be no restriction on the normal derivative of the tangential velocity at the inflow boundary. In practice this means that the instability only really occurs for non-slip boundary conditions when $0 \leqslant \eta \ll 1$, which incidentally is the one choice which, in concert with the no-normal flow condition, means no disturbance kinetic energy is being advected into the domain through the inflow boundary.

2.2. *Half-plane: viscous*

The base state (2.1) is unchanged (by design) when viscosity is introduced, but the linearised disturbance equation (2.2) now includes diffusion of vorticity:

$$\left(\frac{\partial}{\partial t} + y \frac{\partial}{\partial x} + \eta \frac{\partial}{\partial y} \right) \omega = \frac{1}{Re} \nabla^2 \omega. \tag{2.40}$$

Looking for a modal solution $\omega(x, y, t) = \hat{\omega}(y) \exp(\mathrm{i}kx + \sigma t)$ leads to the equation

$$\frac{\mathrm{d}^2 \hat{\omega}}{\mathrm{d}y^2} - Re \, \eta \frac{\mathrm{d}\hat{\omega}}{\mathrm{d}y} - [Re(\sigma + \mathrm{i}ky) + k^2]\hat{\omega} = 0, \tag{2.41}$$

which has the bounded solution (as $y \to \infty$)

$$\hat{\omega} = \mathrm{e}^{Re \, \eta y/2} \mathrm{Ai} \left[\frac{Re\sigma + k^2 + \frac{1}{4}Re^2\eta^2}{(\mathrm{i}kRe)^{2/3}} + (\mathrm{i}kRe)^{1/3}y \right], \tag{2.42}$$

where $\mathrm{Ai}(z)$ is the Airy function bounded as $|z| \to \infty$ with $|\arg(z)| < \pi$. The dispersion relation is then

$$\int_0^\infty \mathrm{e}^{(Re \, \eta/2 - k)\bar{y}} \mathrm{Ai} \left[\frac{Re\sigma + k^2 + \frac{1}{4}Re^2\eta^2}{(\mathrm{i}kRe)^{2/3}} + (\mathrm{i}kRe)^{1/3}\bar{y} \right] \mathrm{d}\bar{y} = 0 \tag{2.43}$$

and instability ($Re(\sigma)$ crosses through 0 to become positive) occurs at a critical inflow $\eta_{crit}(k, Re)$. This integral is actually the same as that treated by Gallet *et al.* (2010) (see their expression (39)) after the transformations

$$N_g^{2/3} := 2^{1/3} \frac{Re \, \eta - 2k}{(kRe)^{1/3}}, \quad a_g = -\left(\frac{4Re}{N_g k^2} \right)^{1/3} (\sigma + k\eta) \tag{2.44a,b}$$

(N_g and a_g from Gallet *et al.* (2010)). For the k of interest ($\leqslant O(1)$), $k\eta \ll |\sigma|$ and we can reuse their critical value of N_g, which has a_g passing through the imaginary axis to give

$$\eta_{crit} = \left(\frac{1}{2}N_g^2 k \right)^{1/3} Re^{-2/3}, \quad \sigma_{crit} = -\left(\frac{N_g k^2}{4Re} \right)^{1/3} a_g, \tag{2.45a,b}$$

where $N_g = 4.57557$ and $a_g = 5.63551\mathrm{i}$ (consistent with Gallet *et al.* (2010), who quote '4.58' and '5.62i' for N_g and a_g, respectively). This threshold η_{crit} tends to zero as $k \to 0$, albeit with the unstable eigenfunction extending a distance $O((kRe)^{-1/3})$

	Asymptotic		Actual	
n	$\tilde{\lambda}$	$\tilde{\eta}_{crit}$	$\tilde{\lambda}$	$\tilde{\eta}_{crit}$
6	35.2992	16.8776	35.183	16.501
5	29.5968	14.2990	29.482	13.885
4	23.8395	11.6711	23.730	11.201
3	18.0097	8.9777	17.9033	8.4197
2	12.0754	6.1886	11.9737	5.4762
1	5.9596	3.2301	5.8938	2.1875

TABLE 2. The six lowest inflow thresholds for instability in the dispersion relation (2.43) with $k = 1$ as $Re \to \infty$ and asymptotic estimates from (2.46) and (2.47).

in the y direction. In terms of connecting this analysis to other problems, there are two notable cases: $k = O(1)$, which is the interesting case in rotating flow where the wavenumber is forced to be an integer by periodicity, and $k = O(Re^{-1})$, which is gives the most unstable disturbance in a domain bounded in y (i.e. a channel, see Nicoud & Angilella 1997). In the former case, $\eta_{crit} = O(Re^{-2/3})$ and the implication from the scaling of the critical frequency is the growth rate away from criticality (i.e. $|\eta - \eta_{crit}| = O(\eta_{crit})$) will be $O(Re^{-1/3})$ or $O(\sqrt{\eta})$, as before. For $k = O(Re^{-1})$, $\eta_{crit} = O(Re^{-1})$, which is consistent with the numerical findings in Nicoud & Angilella (1997) that the threshold 'cross-flow' Reynolds number for inflow instability in their plane Couette flow is independent of the shear Reynolds number.

For any given k, further boundary layer-type instabilities exist as η increases with the first six thresholds listed in table 2 for $k = 1$. Within this 'boundary layer' scaling of $\tilde{\lambda} := -Re^{1/3}\sigma_i$ and $\tilde{\eta}_{crit} := Re^{2/3}\eta_{crit}$ for $k = O(1)$, asymptotic predictions for $\tilde{\lambda} \to \infty$ can be derived following the same route as in the inviscid case. This proves a little more involved, leading to two coupled relations,

$$\tilde{\eta}_{crit} = \tilde{\lambda} \left(\frac{3k}{2} \log(2\pi\tilde{\lambda}/k) - \frac{k}{2} \log \left[\frac{2}{3k \log(2\pi\tilde{\lambda}/k)} \right] \right)^{-1/3}, \qquad (2.46)$$

$$\frac{\tilde{\lambda}^2}{\tilde{\eta}_{crit}} = \frac{1}{2}\pi(8n - 1) \quad n = 1, 2, 3, \ldots, \qquad (2.47)$$

which work reasonably well for $\tilde{\lambda} = O(10)$ given that higher-order terms may only be $\log(\tilde{\lambda})$ smaller.

As in the inviscid case, there are also interior critical layer modes excited for even higher inflows: if the critical layer is at $y = -\sigma_i/k = O(1)$, then

$$\eta_{crit} = |\sigma_i| \left(\frac{2}{kRe \log Re} \right)^{1/3} \gg O(Re^{-2/3}). \qquad (2.48)$$

2.3. *Inflow and suction together: inviscid plane Couette flow with suction*

The half-plane system exhibits boundary inflow instability for all $\eta > 0$. This can be seen by a simple rescaling of space

$$\kappa = \eta^{1+\beta}k, \quad Y = y/\eta^{1+\beta} \quad \text{and} \quad \epsilon = 1/\eta^{\beta}, \qquad (2.49a\text{--}c)$$

where $\beta > 0$, so that the (2.20) becomes

$$(\sigma + \mathrm{i}\kappa Y + \epsilon \partial_Y)(\psi_{YY} - \kappa^2 \psi) = 0, \tag{2.50}$$

which is just the original equation with a new small number ϵ as $\eta \to \infty$. However, this is rather artificial, since the applied pressure gradient also has to be increased with η to maintain the constant shear in y. Resorting to a constant pressure gradient instead now means the shear field decreases as η increases, again making it difficult to draw general conclusions for large η. Introducing another boundary is then the only alternative; and this must be an outflow boundary if the resulting base flow is to be steady and spatially non-developing. The simplest modification is to add an outflow boundary at $y = 1$ which is moving at $\hat{x}$ so that the constant-vorticity basic flow (2.1) is still a solution (Nicoud & Angilella 1997). The equivalent expression to (2.8) is then

$$\hat{\psi}_k(y) = -\int_0^y \frac{\sinh(k\bar{y})}{k \sinh k} \sinh k(1-y) \mathrm{e}^{-(\sigma \bar{y} + \mathrm{i}k\bar{y}^2/2)/\eta} \, \mathrm{d}\bar{y}$$
$$- \int_y^1 \frac{\sinh k(1-\bar{y})}{k \sinh k} \sinh(ky) \mathrm{e}^{-(\sigma \bar{y} + \mathrm{i}k\bar{y}^2/2)/\eta} \, \mathrm{d}\bar{y}, \tag{2.51}$$

with the dispersion relation

$$\int_0^1 \sinh k(1-\bar{y}) \mathrm{e}^{-(\sigma \bar{y} + \mathrm{i}k\bar{y}^2/2)/\eta} \, \mathrm{d}\bar{y} = 0, \tag{2.52}$$

when a non-slip condition is applied at the influx boundary $y = 0$ for $\eta > 0$. This is essentially the same as the half-plane dispersion relation and will have unstable eigenvalues as there is an inflow boundary. The simple rescaling (2.49a−c), however, is disallowed and instability is lost if η becomes too large (see figure 12 of Nicoud & Angilella 1997). This could be interpreted as the stabilising influence of the newly introduced suction boundary ultimately overpowering the destabilising inflow boundary. Further evidence for this comes from the pressure-gradient-free version of this flow, which is also linearly unstable in the presence of viscosity (Doering *et al.* 2000). In this case, the base state varies exponentially in the cross-stream direction (see equation (2.13) of Doering *et al.* 2000) and possesses an area of linear instability in the $(\tan \theta, Re)$ plane (Doering *et al.* (2000, figure 3), where $\tan \theta$ is their proxy for η). The lower boundary of this instability region, $\theta_{lower}(Re)$, plausibly scales like Re^{-1}, which is the viscous threshold for the instability as described in § 2.2, whereas the upper boundary has $\theta_{upper}(Re) = \cot^{-1} 54,370$, which appears to be suction ultimately stabilising the flow (Hocking 1974).

3. 2D swirling flow with radial inflow

We now add curvature to the discussion and consider the basic, steady, axisymmetric solution

$$\boldsymbol{U} = -\frac{\eta}{r}\hat{\boldsymbol{r}} + r\Omega(r)\hat{\boldsymbol{\theta}} \tag{3.1}$$

between two boundaries at $r = 1$ and $r = a\,(> 1)$ with $\Omega(1) = 1$ (i.e. the inner radius r^* and the angular velocity Ω^* there are used as length and inverse time

scales respectively) and $0 < \eta$ so that there is a radial inflow. The 2D Navier–Stokes equations for the deviation $\boldsymbol{u}$ of the total flow $\boldsymbol{u}_{tot}$ from the basic solution (3.1),

$$\boldsymbol{u} := \boldsymbol{u}_{tot} - \boldsymbol{U} = u(r, \theta, t)\hat{\boldsymbol{r}} + v(r, \theta, t)\hat{\boldsymbol{\theta}} \tag{3.2}$$

are

$$\left(\frac{\partial}{\partial t} + \Omega \frac{\partial}{\partial \theta} - \frac{\eta}{r} \frac{\partial}{\partial r}\right) u + \frac{\eta u}{r^2} - 2\Omega v + \boldsymbol{u} \cdot \nabla u - \frac{v^2}{r} + \frac{\partial p}{\partial r}$$
$$= \frac{1}{Re} \left[\left(\nabla^2 - \frac{1}{r^2}\right) u - \frac{2}{r^2} \frac{\partial v}{\partial \theta}\right] \tag{3.3}$$

$$\left(\frac{\partial}{\partial t} + \Omega \frac{\partial}{\partial \theta} - \frac{\eta}{r} \frac{\partial}{\partial r}\right) v + u \frac{\mathrm{d}(r\Omega)}{\mathrm{d}r} - \frac{\eta v}{r^2} + \Omega u + \boldsymbol{u} \cdot \nabla v + \frac{uv}{r} + \frac{1}{r} \frac{\partial p}{\partial \theta}$$
$$= \frac{1}{Re} \left[\left(\nabla^2 - \frac{1}{r^2}\right) v + \frac{2}{r^2} \frac{\partial u}{\partial \theta}\right] \tag{3.4}$$

together with incompressibility

$$\frac{1}{r} \frac{\partial (ru)}{\partial r} + \frac{1}{r} \frac{\partial v}{\partial \theta} = 0, \tag{3.5}$$

where

$$Re := \frac{r^{*2} \Omega^*}{\nu} \tag{3.6}$$

and ν is the kinematic viscosity. Introducing a stream function

$$u = \frac{1}{r} \frac{\partial \psi}{\partial \theta}, \quad v = -\frac{\partial \psi}{\partial r}, \tag{3.7a,b}$$

reduces the system (3.3)–(3.5) to

$$\left(\frac{\partial}{\partial t} + \Omega(r) \frac{\partial}{\partial \theta} - \frac{\eta}{r} \frac{\partial}{\partial r}\right) \Delta \psi = \frac{1}{r} \frac{\mathrm{d}Z}{\mathrm{d}r} \frac{\partial \psi}{\partial \theta} + \frac{1}{Re} \Delta^2 \psi + \frac{1}{r} J(\psi, \Delta \psi), \tag{3.8}$$

where the Jacobian is defined as

$$J(A, B) := \frac{\partial A}{\partial r} \frac{\partial B}{\partial \theta} - \frac{\partial A}{\partial \theta} \frac{\partial B}{\partial r} \tag{3.9}$$

and

$$Z := \frac{1}{r} \frac{\mathrm{d}(r^2 \Omega)}{\mathrm{d}r} \tag{3.10}$$

is the vorticity of the basic flow (3.1). There are two special cases where the gradient of the vorticity vanishes: uniform rotation ($\Omega = 1$ so $Z = 2$) and irrotational flow ($\Omega = 1/r^2$ with $Z = 0$), originally considered by Ilin & Morgulis (2013).

3.1. *Basic state*

There are two usual scenarios: (1) the swirl field $\Omega(r)$ is set by the boundary conditions as in Taylor–Couette flow or (2) the swirl field is determined by an imposed body (gravitational) force as in the astrophysical context. In the former, the swirl is determined by the azimuthal momentum equation given a radial flow with the radial momentum equation determining the pressure field. For example Ilin & Morgulis (2013) discuss the inviscid, irrotational, axisymmetric Taylor–Couette-like flow

$$\Omega_{inviscid} := \frac{1}{r^2},\tag{3.11}$$

which is the only possibility with axisymmetric radial flow (recall $\Omega(1) = 1$ by non-dimensionalisation). Gallet *et al.* (2010) consider the viscous Taylor–Couette situation, where possible base flows form a one-parameter family

$$\Omega_{TC} = \frac{1-A}{r^2} + Ar^{-\eta Re}\tag{3.12}$$

with A a constant set by the motion of the outer cylinder, which is generally rotational ($Z = A(2 - \eta Re)r^{-\eta Re}$). In the (latter) astrophysical context, the acting gravitational (body) force sets the swirl field (via the radial momentum equation), which then sets the radial flow by the need to balance ensuing azimuthal viscous stresses. The focus here is on the latter situation, and we consider the general set of profiles

$$\Omega = r^\alpha\tag{3.13}$$

in order to understand how robust the boundary inflow instability is. Profiles with $-2 < \alpha < 0$ have angular momentum increasing with radius and are thus Rayleigh-stable (Rayleigh 1917). The gradient of the vorticity $dZ/dr = \alpha(\alpha + 2)\Omega/r$ also does not change sign across the domain $r \in [1, a]$, so that the flow is inviscidly stable (for disturbances which vanish at $r = 1$ and a) by a rotating flow analogue of Rayleigh's inflexion-point theorem (Rayleigh 1880). Particularly interesting choices for α are $\alpha = -3/2$, which is the Keplerian profile for a thin accretion disk due to the radial force balance

$$-r\Omega^2 = -\frac{GM}{r^2},\tag{3.14}$$

(where G is the gravitational constant and M the mass of the central object), and $\alpha = -1$, which is used to model spiral galaxies. Since we work with deviations away from the basic state, the exact body force required to maintain the underlying rotation profile is not explicitly needed in what follows. In contrast to the Taylor–Couette situation, the azimuthal component of the Navier–Stokes equations forces the existence of a small radial flow

$$U = \frac{1}{Re}\left(\frac{\partial}{\partial r}\log\left|\frac{\partial}{\partial r}(r^2\Omega)\right| - \frac{1}{r}\right) = \frac{\alpha}{Re}\frac{1}{r},\tag{3.15}$$

which is an inflow if $d\Omega/dr < 0$ ($\alpha < 0$). Studying the consequences of this small accretion flow is the motivation for this work.

3.2. *2D inviscid swirling flow with* $dZ/dr = 0$

We study the simplest case of vanishing vorticity gradient in the base flow first ($dZ/dr = 0$), so $\Omega = 1/r^2$ or 1, to show how the analysis mirrors that in the half-plane case. The case of uniform rotation $\Omega = 1$ initially looks uninteresting because the base flow needs an azimuthal as well as a radial body force to maintain it (since $\alpha = 0$ in (3.15)). But it is worth considering, as then only the enforced radial inflow creates shear in the base flow and the question is whether this is enough to generate instability. The inviscid, linearised governing equation (3.8) is just

$$\left(\frac{\partial}{\partial t} + \Omega(r) \frac{\partial}{\partial \theta} - \frac{\eta}{r} \frac{\partial}{\partial r} \right) \omega = 0, \tag{3.16}$$

which is the 'curved' analogue of (2.2) and again third order rather than the usual second order. As before, the solution can be written down using characteristics as

$$\omega(r, \theta, t) = \omega_0 \left(r^2 + 2\eta t, \theta + \frac{1}{\eta} \int_{\sqrt{r^2 + 2\eta t}}^{r} \Omega(r^*) r^* \, dr^* \right), \tag{3.17}$$

where $\omega_0(r, \theta)$ is the initial vorticity. After a discrete Fourier transform, the $e^{im\theta}$ component is

$$\left(\frac{1}{r} \frac{\partial}{\partial r} r \frac{\partial}{\partial r} - \frac{m^2}{r^2} \right) \psi_m(r, t) = g(r^2 + 2\eta t) \exp \left(\frac{im}{\eta} \int_{\sqrt{r^2 + 2\eta t}}^{r} \Omega(r^*) r^* \, dr^* \right), \tag{3.18}$$

where g is an arbitrary function. For modal growth, $\psi_m(r, t)$ should depend on t only through an $\exp(\sigma t)$ factor for some complex constant σ, which forces

$$g(\xi) = B \exp \left(\frac{\sigma \xi}{2\eta} - \frac{im}{\eta} \int_{\sqrt{\xi}}^{a} \Omega(r^*) r^* \, dr^* \right) \tag{3.19}$$

(B is some constant which can be set to 1 providing the influx boundary conditions do not force $B = 0$) and, letting $\psi_m(r, t) = \hat{\psi}_m(r) \exp(\sigma t)$, then

$$\left(\frac{1}{r} \frac{\partial}{\partial r} r \frac{\partial}{\partial r} - \frac{m^2}{r^2} \right) \hat{\psi}_m(r) = \exp \left(\frac{\sigma r^2}{2\eta} - \frac{im}{\eta} \int_{r}^{a} \Omega(r^*) r^* \, dr^* \right). \tag{3.20}$$

This has the solution

$$\hat{\psi}_m(r) = \int_{1}^{r} G_+(r, \bar{r}; a, m) \exp \left(\frac{\sigma \bar{r}^2}{2\eta} - \frac{im}{\eta} \int_{\bar{r}}^{a} \Omega(r^*) r^* \, dr^* \right) d\bar{r}$$
$$+ \int_{r}^{a} G_-(r, \bar{r}; a, m) \exp \left(\frac{\sigma \bar{r}^2}{2\eta} - \frac{im}{\eta} \int_{\bar{r}}^{a} \Omega(r^*) r^* \, dr^* \right) d\bar{r}, \tag{3.21}$$

where

$$G_-(r, \bar{r}; a, m) := \frac{\bar{r}}{2m(a^{2m} - 1)} \left(\bar{r}^m - \frac{a^{2m}}{\bar{r}^m} \right) \left(r^m - \frac{1}{r^m} \right) \tag{3.22}$$

$$G_+(r, \bar{r}; a, m) := \frac{\bar{r}}{2m(a^{2m} - 1)} \left(\bar{r}^m - \frac{1}{\bar{r}^m} \right) \left(r^m - \frac{a^{2m}}{r^m} \right) \tag{3.23}$$

make up the Green's function built around the two (usual) no-normal-velocity boundary conditions that $\hat{\psi}_m(1) = 0$ and $\hat{\psi}_m(a) = 0$. Imposing the third boundary condition of non-slip, $\mathrm{d}\hat{\psi}_m(a)/\mathrm{d}r = 0$, gives the dispersion relation

$$\int_1^a (\bar{r}^{m+1} - \bar{r}^{1-m}) \exp\left(\frac{\sigma \bar{r}^2}{2\eta} - \frac{\mathrm{i}m}{\eta} \int_{\bar{r}}^a \Omega(r^*) r^* \, \mathrm{d}r^* \right) \mathrm{d}\bar{r} = 0. \qquad (3.24)$$

For $\Omega = 1/r^2$ this is exactly expression (5.3) from Ilin & Morgulis (2013), which they establish has unstable eigenvalues. The energy budget for an infinitesimal 2D disturbance,

$$\frac{\mathrm{d}}{\mathrm{d}t} \left\langle \frac{1}{2} \boldsymbol{u}^2 \right\rangle = \eta \left\langle \frac{v^2 - u^2}{r^2} \right\rangle - \eta \int_0^{2\pi} \frac{1}{2} v^2 \bigg|_{r=1} \mathrm{d}\theta - \left\langle ruv \frac{\mathrm{d}\Omega}{\mathrm{d}r} \right\rangle, \qquad (3.25)$$

where $\langle\ \rangle := \int_0^{2\pi} \int_1^a r \, \mathrm{d}r \, \mathrm{d}\theta$, $u = 0$ at $r = 1$ and $u = v = 0$ at $r = a$, clearly shows that enhanced growth rates of $O(\sqrt{\eta})$ are possible only if $\mathrm{d}\Omega/\mathrm{d}r$ is non-zero somewhere in the domain, emphasising the importance of azimuthal shear. In particular, for $\Omega = 1$, the last term drops, so that any instability can have a growth rate of only $O(\eta)$ at best. In fact, the dispersion relation appears only to have stable solutions, indicating that boundary inflow and just the shear due to the radial inflow are insufficient to drive any instability.

The $\eta \to 0$ asymptotic analysis for $\Omega = 1/r^2$ mirrors that in the half-plane case with the saddle point at $\sigma + \mathrm{i}m\Omega(r_s) = 0$. For the boundary layer scenario, adopting the scalings

$$\sigma = -\mathrm{i}m\Omega(a) + \sqrt{\eta\chi/a}\,(\hat{\sigma}_r + \mathrm{i}\hat{\sigma}_i) + O(\eta), \qquad (3.26)$$

$$z := \sqrt{a\chi}\,\frac{(a-r)}{\sqrt{\eta}}, \qquad (3.27)$$

where $\chi := -(m\Omega'(a))/2$ ($\Omega'(r) < 0$ for cases of interest) and z is a boundary layer variable (as before), retrieves (2.15), which has the unstable eigenvalues $\hat{\sigma}$ listed in table 1: there is instability with growth rates $O\left(\sqrt{\eta(-m\Omega'(a)/(2a))}\right)$.

For the critical layer scenario, the appropriate eigenvalue scaling is again (2.11), which, given $\sigma + \mathrm{i}m\Omega(r_s) = 0$, leads to the expansion

$$r_s := R_s + \frac{\mathrm{i}\delta(\eta)\tilde{\sigma}_r}{m\Omega'(R_s)} + \cdots \qquad (3.28)$$

for the saddle point position, where $\sigma_i = -m\Omega(R_s)$ defines R_s. The balance between the leading contribution from the saddle point at $r = r_s$ (first term) and the endpoint $r = a$ (second term) is then

$$\frac{\sqrt{-\mathrm{i}\eta\,\pi}(r_s^{m+1} - r_s^{1-m})}{\sqrt{-\frac{1}{2}mr_s\Omega'(r_s)}} \exp\left(\frac{\sigma r_s^2}{2\eta} - \frac{\mathrm{i}m}{\eta} \int_{r_s}^a \Omega(r^*) r^* \, \mathrm{d}r^* \right)$$

$$- \frac{\mathrm{i}\eta\,(a^m - a^{-m})}{(\sigma_i + m\Omega(a))} \exp\left(\frac{\sigma a^2}{2\eta} \right) = 0, \qquad (3.29)$$

which leads to the frequency condition

$$\mathrm{Arg}\left\{ \exp\left[\mathrm{i}\left(\frac{\sigma_i(R_s^2 - a^2)}{2\eta} - \frac{m}{\eta} \int_{R_s}^a \Omega(r^*) r^* \, \mathrm{d}r^* + \frac{\pi}{4} \right) \right] \right\} = 0 \qquad (3.30)$$
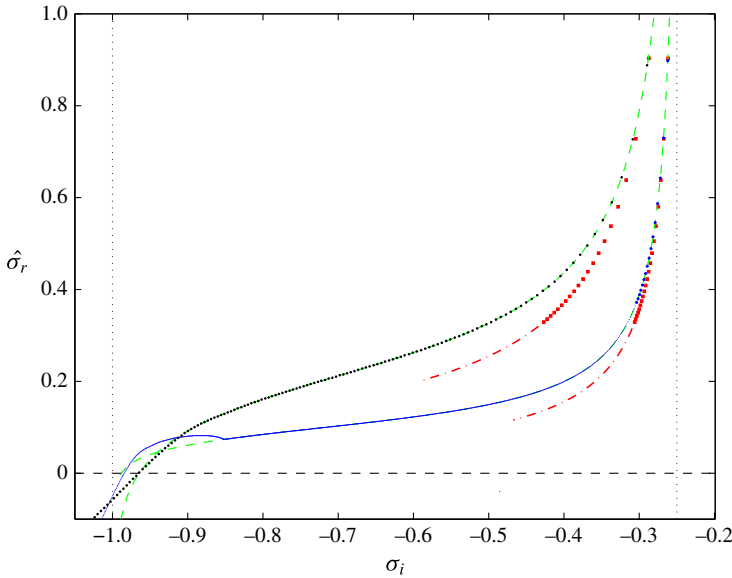
FIGURE 2. (Colour online) Inviscid 2D instabilities for $\alpha = -2$, $m = 1$ and $a = 2$ with scaled growth rate $\hat{\sigma}_r = \sigma_r / \sqrt{-m\eta\Omega'(a)/(2a)}$ plotted against frequency σ_i. The right (left) vertical dashed line is $\sigma_i = -m\Omega(a)$ ($\sigma_i = -m\Omega(1)$). The eigenvalues from a full 2D eigenvalue calculation are shown as (the upper) black dots for $\eta = 10^{-3}$ ($N = 1000$) and (the lower) blue dots for $\eta = 10^{-4}$ (since $N = 4000$ here, the 15 most unstable eigenvalues are marked with a normal-sized dot and the rest by smaller blue dots). The red squares are the 20 most unstable modes from the boundary layer asymptotics (§ 3.2) with the dash-dot red line tracing the path of the rest (eigenvalues calculated from the boundary layer equation (2.22) are indistinquishable from the asymptotics at this scale). The green dashed lines are the critical layer asymptotic expression (3.31) with $\eta = 10^{-3}$ and 10^{-4} plugged in and appropriately rescaled: $\hat{\sigma}_r = \delta_1 \tilde{\sigma}_r \sqrt{(2a)/(-m\eta\Omega'(a))}$ and $\sigma_i = -m\Omega(R_s)$ with R_s taken over $[1, a]$. Notice that, at $\eta = 10^{-4}$, even $N = 4000$ struggles to fully resolve the critical layer eigenvalues near the inner radius – see the hump in the numerical data which breaks the otherwise excellent correspondence with the asymptotic prediction. This hump is delayed to lower σ_i if N is increased until it eventually disappears – e.g. the $\eta = 10^{-3}$ curve.

and growth rate

$$\delta\tilde{\sigma}_r = \frac{\eta}{(a^2 - R_s^2)} \left[\log\left(\frac{1}{\eta}\right) + 2\log\left(\frac{(R_s^{m+1} - R_s^{1-m})(-\sigma_i - m\Omega(a))\sqrt{2\pi}}{(a^m - a^{-m})\sqrt{-mR_s\Omega'(R_s)}}\right) + o(1) \right]. \tag{3.31}$$

Figure 2 shows that this performs well for numerical calculations with $\eta = 10^{-3}$ and 10^{-4}. The most unstable boundary layer eigenfunction for $\eta = 10^{-3}$ is shown in figure 3 along with a critical layer mode with $\sigma_i \approx -0.5$ which is typical.

3.3. *2D inviscid swirling flow with* $\mathrm{d}Z/\mathrm{d}r \neq 0$

The asymptotic analysis can easily be extended to treat more general rotation profiles $\Omega(r)$ where the gradient of vorticity is non-zero. The idea here is to assume some small viscosity to induce a radial inflow (via (3.15)) and then to show that the inviscid
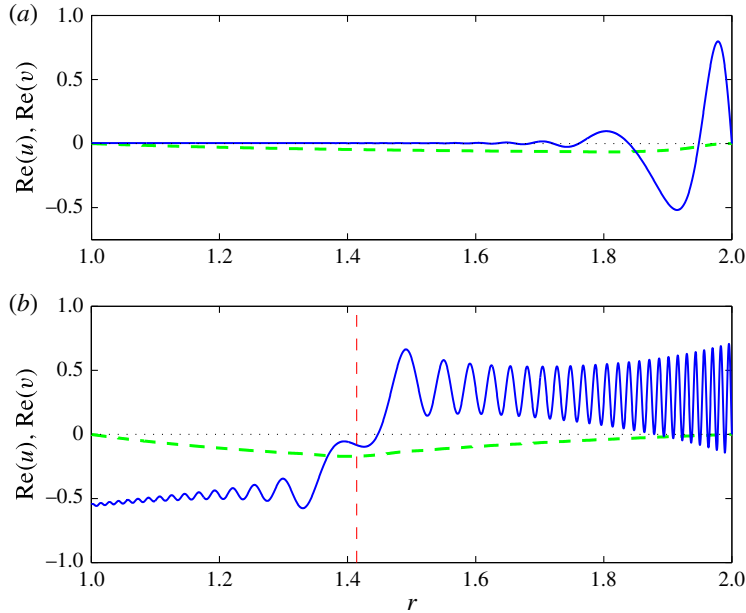
FIGURE 3. (Colour online) The most unstable boundary layer eigenfunction (*a*) and an unstable critical layer eigenfunction with $\sigma_i \approx -0.5$ (*b*) for $\eta = 10^{-3}$, $m = 1$, $a = 2$ and $\alpha = -2$. In both, the green dashed line is $\text{Re}(u)$ and the blue solid line is $\text{Re}(v)$. The critical layer position is shown as a red dashed line for the critical layer eigenfunction.

instability mechanism is robust to the exact form of the azimuthal flow (e.g. whether it has a vorticity gradient or not). So, taking the linear, inviscid version of perturbation equation (3.8) and inserting the usual ansatz $\psi(r, \theta, t) = \psi(r) \exp(im\theta + \sigma t)$ gives

$$\left(\sigma + im\Omega(r) - \frac{\eta}{r}\frac{d}{dr}\right)\mathscr{L}\psi = \frac{im\psi}{r}\frac{dZ}{dr}, \qquad (3.32)$$

where

$$\mathscr{L} := \frac{d^2}{dr^2} + \frac{1}{r}\frac{d}{dr} - \frac{m^2}{r^2}. \qquad (3.33)$$

The $\eta = 0$ problem

$$(\sigma + im\Omega(r))\mathscr{L}\psi = \frac{im\psi}{r}\frac{dZ}{dr} \qquad (3.34)$$

subject to the two boundary conditions $\psi(1) = \psi(a) = 0$ seems to have no discrete modal solutions for the profiles $\Omega = r^\alpha$ studied here. This is easily proved for the special choices $\alpha = 0$ and -2 (so $dZ/dr = 0$) (Ilin & Morgulis 2013), but is only suggested by numerical evidence generally. This observation is significant because it forces a non-standard singular perturbation analysis in which the additional flow component for $\eta \neq 0$ has to contribute at leading order to help satisfy one of these two boundary conditions rather than just 'fixing up' the third boundary condition.

The analysis of the boundary layer instability is exactly the same as the $\Omega = 1/r^2$ case because the presence of a vorticity gradient does not affect the boundary layer problem at leading order. So the growth rate $\text{Re}(\sigma)$ scales like $\sqrt{((-m\Omega'(a)\eta)/2)/a}$

with azimuthal wavenumber m, local shear at the boundary $-\Omega'(a) > 0$, and radial flow η. The key point is that the boundary layer instability only depends on the shear at the inflow boundary.

The analysis for the critical layer instability also proceeds in a similar fashion, with one key difference: the problem for the large-scale flow is now complicated by a non-vanishing vorticity gradient, but this only has a secondary effect: dZ/dr affects the growth rate at $O(\eta)$ rather than at the leading $O(\eta \log 1/\eta)$ level. The starting point is the ansatz

$$\sigma = i\sigma_i + \delta\tilde{\sigma}_r\sqrt{\chi/R_s}, \tag{3.35}$$

where $\sigma_i = -m\Omega(R_s)$ and R_s is the position of the critical layer, $\chi := -m\Omega'(R_s)/2$ and $\delta \ll \sqrt{\eta}$. In the critical layer

$$(-\delta\tilde{\sigma}_r/\sqrt{\eta} + 2i\xi + \partial_\xi)\hat{\psi}_{\xi\xi} = 0 \tag{3.36}$$

to leading order, where $\xi := \sqrt{R_s\chi/\eta}(r - R_s)$. This has the arbitrarily normalised solution

$$\hat{\psi}_{\xi\xi} = e^{\delta\tilde{\sigma}\xi/\sqrt{\eta} - i\xi^2}. \tag{3.37}$$

Matching this to ψ_{rr} outside the critical layer requires the WKB solution

$$\psi^{WKB} = \frac{-R_s\chi\,\eta}{m^2r^2[\Omega(r) - \Omega(R_s)]^2}\exp\left[\frac{im}{\eta}\int_{R_s}^r \bar{r}(\Omega(\bar{r}) - \Omega(R_s))\,d\bar{r} + \sqrt{\frac{\chi}{R_s}}\frac{\delta\tilde{\sigma}(r^2 - R_s^2)}{2\eta}\right] \tag{3.38}$$

to exist there. There are two other 'outer' large-scale solutions either side of the critical layer which solve

$$[\Omega(r) - \Omega(R_s)]\mathscr{L}\psi = \frac{\psi_0}{r}\frac{dZ}{dr} \tag{3.39}$$

and together accommodate the jump conditions

$$[u]_-^+ = 0 \quad \text{and} \quad [v]_-^+ = \sqrt{\frac{\pi R_s\chi}{i\eta}} \tag{3.40a,b}$$

across the critical layer (found by integrating (3.37) twice) and the no-normal velocity boundary conditions at $r = 1$ and $r = a$. Then, as in § 2.1.2, balancing the large-scale component of the azimuthal velocity with that from the WKB solution at $r = a$ furnishes the growth rate and dispersion relation for the frequency. Only the higher-order $O(\eta)$ part of the growth rate depends on dZ/dr, or indeed $\Omega(r)$, whereas the leading $O(\eta \log 1/\eta)$ part does not (note χ, which contains $\Omega'(R_s)$, needs to be non-zero, but otherwise scales out).

3.4. *Viscous asymptotics for $0 < \eta \ll 1$ for the boundary layer instability*

The inviscid asymptotics can be generalised to include viscosity, which we do here just for the more dangerous boundary layer instability, as this defines the viscous threshold for instability. In the absence of any other physics, the radial inflow is set by the viscosity present via (3.15). However, to extract the scaling law for the viscous instability threshold for more generally maintained radial inflows, we ignore this connection and assume η can vary independently of Re. It is a simple

matter to reinstate this connection later to establish stability or instability for a purely hydrodynamic situation. On this basis, the linearised disturbance equation for $\psi = \psi(r)\mathrm{e}^{\mathrm{i}m\theta+\sigma t}$ is

$$\left(\sigma + \mathrm{i}m\Omega(r) - \frac{\eta}{r}\frac{\mathrm{d}}{\mathrm{d}r}\right)\mathscr{L}\psi = \frac{\mathrm{i}m}{r}\frac{\mathrm{d}Z}{\mathrm{d}r}\psi + \frac{1}{Re}\mathscr{L}^2\psi. \tag{3.41}$$

Setting $\sigma + \mathrm{i}m\Omega(a) = \epsilon\hat{\sigma}$, with $\hat{\sigma} = O(1)$, and where ϵ is the width of the boundary layer at $r = a$, and balancing the frequency, inflow and viscous terms (Gallet *et al.* 2010)

$$\hat{\sigma}/\epsilon \sim \eta/\epsilon^3 \sim \frac{1}{\epsilon^4 Re} \tag{3.42}$$

leads to $\epsilon = Re^{-1/3}$ and $\eta = \hat{\eta}\epsilon^2$, where $\hat{\eta} = O(1)$. Defining the boundary layer variable

$$y := \frac{\sqrt{\chi}}{\sqrt{\hat{\eta}/a}}\left(\frac{a-r}{\epsilon}\right) \tag{3.43}$$

with, recall, $\chi := -m\Omega'(a)/2$ and adopting the standard boundary layer decomposition $\psi = \psi_0 + \hat{\psi}_0 + \epsilon(\psi_1 + \hat{\psi}_1) + \cdots$, leads to the boundary layer equation at $r = a$ (the boundary layer at $r = 1$ is very weak and can be ignored at leading order)

$$\left[\frac{\mathrm{d}^2}{\mathrm{d}y^2} - N\frac{\mathrm{d}}{\mathrm{d}y} - N(\hat{\sigma}_0 + 2\mathrm{i}y)\right]\frac{\mathrm{d}^2\hat{\psi}_0}{\mathrm{d}y^2} = 0 \tag{3.44}$$

with

$$N := \frac{(\hat{\eta}/a)^{3/2}}{\chi^{1/2}} \quad \text{and} \quad \hat{\sigma}_0 := \hat{\sigma}/(N\chi^2)^{1/3}. \tag{3.45a,b}$$

This is exactly equation (36) in Gallet *et al.* (2010) if their 'a' $:= -\hat{\sigma}_0$. The solution which vanishes for $y \to \infty$ is

$$\frac{\mathrm{d}^2\hat{\psi}_0}{\mathrm{d}y^2} = \mathrm{e}^{Ny/2}\mathrm{Ai}\left[\frac{N^{1/3}\hat{\sigma}_0}{(2\mathrm{i})^{2/3}} + \frac{N^{4/3}}{4(2\mathrm{i})^{2/3}} + (2\mathrm{i})^{1/3}N^{1/3}y\right], \tag{3.46}$$

where Ai is the Airy function. Imposing the further non-slip condition $\mathrm{d}\hat{\psi}_0/\mathrm{d}y = 0$ at $y = 0$ defines the dispersion relation

$$\int_0^\infty \mathrm{e}^{Ny/2}\mathrm{Ai}\left[\frac{N^{1/3}\hat{\sigma}_0}{(2\mathrm{i})^{2/3}} + \frac{N^{4/3}}{4(2\mathrm{i})^{2/3}} + (2\mathrm{i})^{1/3}N^{1/3}y\right]\mathrm{d}y = 0. \tag{3.47}$$

The onset of instability is found for $N = N_c$ where $\mathrm{Re}(\hat{\sigma}_0)$ passes through zero (in the positive direction). Numerically, it is better to solve (3.44) directly as an eigenvalue problem rather than treat this integral equation (see appendix A). We find $N_c = 4.57557$ and $\hat{\sigma}_0 = -5.63551\mathrm{i}$, which is consistent with Gallet *et al.* (2010): the threshold radial flow rate for instability is

$$\eta_{crit} = aN_c^{2/3}\chi^{1/3}Re^{-2/3}. \tag{3.48}$$

Since the viscously induced radial flow in an accretion disk is $O(Re^{-1}) \ll \eta_{crit}$, the instability is not expected to be triggered unless it is substantially subcritical. Whether this is the case will be considered below in §6 after we examine the effect of introducing some extra physics to the instability.

4. 2D compressible swirling flow with radial inflow

From the astrophysical perspective, an important ingredient so far missing from the models considered is compressibility. Adding this extra physics also provides an opportunity to test the robustness of the boundary inflow instability. As the simplest model to include compressibility, we consider the fluid to be an isothermal perfect gas, so that pressure p and density ρ are simply related by $p = c^2 \rho$, where c^2 is the isothermal speed of sound. The divergence-free flow

$$\boldsymbol{U} = -\frac{\eta}{r}\hat{\boldsymbol{r}} + \frac{1}{r}\hat{\boldsymbol{\theta}} \tag{4.1}$$

is a steady solution of the inviscid 2D momentum equations

$$U\frac{\mathrm{d}U}{\mathrm{d}r} - \frac{V^2}{r} + \frac{1}{\rho_0}\frac{\mathrm{d}p_0}{\mathrm{d}r} = -\frac{1}{r^3} \tag{4.2}$$

$$U\frac{\mathrm{d}V}{\mathrm{d}r} + \frac{UV}{r} = 0, \tag{4.3}$$

where $\rho_0(r) = \rho(r)/\rho(1)$, so the density is non-dimensionalised by its value at the inner radius r^*, and $p_0(r) = p(r)/(\rho(1)r^{*2}\Omega^{*2})$. This non-dimensionalisation means $p_0 = \delta\rho_0$, where $\delta := c^2/(r^{*2}\Omega^{*2})$ and $\delta \to \infty$ is the incompressible limit. In a thin Keplerian disk, however, the basic rotation speed is highly supersonic, so $\delta \ll 1$ (e.g. p. 87, Frank, King & Raine 1985) and $\eta \sim Re^{-1} \ll \delta$, so the question is whether the instability still operates for $\eta \ll \delta \ll 1$.

In the laboratory, the body force on the right-hand side of (4.2) would be absent, leaving only the pressure gradient to drive the centripetal acceleration. In an accretion disk, however, the gravitational attraction to the central object plays this role and the pressure gradient only exists to balance the much smaller radial advection term. To model this latter situation, a body force is included (albeit here with different radial dependence so $\Omega := 1/r^2$) to support the irrotational basic state needed to satisfy (4.3) in the absence of viscosity. The pressure gradient is then only $O(\eta^2)$. With this, the density drifts very slowly as mass balance requires

$$\frac{\partial \rho_0}{\partial t} = \frac{\eta}{r}\frac{\partial \rho_0}{\partial r} \sim O\left(\frac{\eta^3}{\delta}\right)\rho_0. \tag{4.4}$$

Given the instability being studied here develops over a much shorter $O(1/\sqrt{\eta})$ time scale, both this secular change and the very small pressure gradient can be ignored, i.e. it is valid to set $\rho_0 = 1$ and $p_0 = \delta$ (formally, this is because $\boldsymbol{u}_1 \cdot \nabla\rho_0 \ll \boldsymbol{U} \cdot \nabla\rho_1$ and $\rho_1/\rho_0^2\,\mathrm{d}p_0/\mathrm{d}r \ll 1/\rho_0\,\mathrm{d}p_1/\mathrm{d}r$). After doing this, the 2D linearised disturbance equations are then

$$\left(\sigma + im\Omega(r) - \frac{\eta}{r}\frac{\mathrm{d}}{\mathrm{d}r}\right)u_1 = -\frac{\eta}{r^2}u_1 + 2\Omega v_1 - \frac{\mathrm{d}p_1}{\mathrm{d}r}, \tag{4.5}$$

$$\left(\sigma + im\Omega(r) - \frac{\eta}{r}\frac{\mathrm{d}}{\mathrm{d}r}\right)v_1 = \frac{\eta}{r^2}v_1 - Zu_1 - \frac{im}{r}p_1, \tag{4.6}$$

$$\left(\sigma + im\Omega(r) - \frac{\eta}{r}\frac{\mathrm{d}}{\mathrm{d}r}\right)p_1 = -\delta\nabla \cdot \boldsymbol{u}_1, \tag{4.7}$$

δ	$\text{Im}(\hat{\sigma})$	$\text{Re}(\hat{\sigma})$
∞	-4.7795	0.9114
100	-4.7795	0.9114
1	-4.7796	0.9092
10^{-1}	-4.7784	0.9290
10^{-2}	-4.7793	0.9081
10^{-3}	-4.7748	0.9052
10^{-4}	-4.0979	1.1839

TABLE 3. The most unstable eigenvalue $\hat{\sigma}$ for the eigenvalue problem (4.5)–(4.7) with $\eta = 10^{-4}$ and various degrees of compressibility. The presence of δ only becomes significant when it is $\leqslant O(\eta)$.

where the disturbance fields $\boldsymbol{u}_1$ and p_1 are taken proportional to $e^{im\theta + \sigma t}$ ($p_1 = \delta\rho_1$). Assuming the boundary layer scalings of §3.2,

$$\sigma = -im\Omega(a) + \sqrt{\frac{-m\eta\Omega'(a)}{2a}}\,\hat{\sigma} + \cdots, \quad \xi = (a - r)\sqrt{\frac{-ma\Omega'(a)}{2\eta}}, \quad (4.8a,b)$$

$$(u_1, v_1, p_1) = \left(\sqrt{\eta}\hat{u}, \sqrt{\frac{-ma\Omega'(a)}{a}}\,\hat{v}, \sqrt{\eta}\hat{p}\right). \quad (4.9)$$

The equations become, to leading order in η,

$$0 = 2\Omega\hat{v} + \frac{d\hat{p}}{d\xi}, \quad (4.10)$$

$$-\frac{1}{2}m\Omega'(a)\left(\hat{\sigma} + 2i\xi + \frac{d}{d\xi}\right)\hat{v} = -Z(a)\hat{u} - \frac{im}{a}\hat{p}, \quad (4.11)$$

$$\left(\hat{\sigma} + 2i\xi + \frac{d}{d\xi}\right)\hat{p} = -\frac{\delta}{a\eta}\left(-\frac{d\hat{u}}{d\xi} + \frac{im\hat{v}}{a}\right), \quad (4.12)$$

which can be reduced to the equation

$$\left(\hat{\sigma} + 2i\xi + \frac{d}{d\xi}\right)\frac{d\hat{v}}{d\xi} = \frac{\eta}{\delta}\left[\frac{2aZ(a)}{m\Omega'(a)}\right]\left(\hat{\sigma} + 2i\xi + \frac{d}{d\xi}\right)\hat{p}. \quad (4.13)$$

This suggests that the incompressible limit $\delta \to \infty$ which recovers the boundary layer equation (2.22) still holds provided $\eta \ll \delta$, and this is confirmed by numerical computations: for example, see table 3.

5. 3D linear instability

We now study three-dimensional disturbances. Adopting the ansatz $\boldsymbol{u}(r, \theta, z, t) = \boldsymbol{u}(r)e^{i(m\theta + kz) + \sigma t}$, the linearised inviscid governing equations are

$$\left(\sigma + im\Omega(r) - \frac{\eta}{r}\frac{d}{dr}\right)u + \frac{\eta}{r^2}u - 2\Omega v + \frac{dp}{dr} = 0, \quad (5.1)$$

$$\left(\sigma + im\Omega(r) - \frac{\eta}{r}\frac{\mathrm{d}}{\mathrm{d}r}\right)v - \frac{\eta}{r^2}v + Zu + \frac{im}{r}p = 0, \tag{5.2}$$

$$\left(\sigma + im\Omega(r) - \frac{\eta}{r}\frac{\mathrm{d}}{\mathrm{d}r}\right)w + ikp = 0, \tag{5.3}$$

$$\frac{1}{r}\frac{\mathrm{d}(ru)}{\mathrm{d}r} + \frac{im}{r}v + ikw = 0. \tag{5.4}$$

In contrast to the 2D situation, discrete neutral modes start to emerge for $k \neq 0$ in the absence of radial flow. For example, in the case of axisymmetric modes the equations (5.1)–(5.4) boil down to the second-order ODE for u

$$\frac{\mathrm{d}^2 u}{\mathrm{d}r^2} + \frac{1}{r}\frac{\mathrm{d}u}{\mathrm{d}r} - \left(\frac{2k^2}{\sigma^2}Z\Omega + k^2 + \frac{1}{r^2}\right)u = 0. \tag{5.5}$$

There are two profiles $\Omega(r)$ which make this just Bessel's equation: $\Omega = 1$ ($\alpha = 0$) and $\Omega = 1/r$ ($\alpha = -1$). In the former, uniform rotation case, eigensolutions are axisymmetric Poincaré modes (Greenspan 1968). In the latter case, the general solution is $u = A\mathrm{J}_\nu(ikr) + B\mathrm{Y}_\nu(ikr)$, where $\nu := \sqrt{1 + 2k^2/\sigma^2}$, with the dispersion relation (since $u(1) = u(a) = 0$)

$$\mathrm{J}_\nu(ik)\,\mathrm{Y}_\nu(ika) = \mathrm{Y}_\nu(ik)\,\mathrm{J}_\nu(ika). \tag{5.6}$$

This has purely imaginary eigenvalues $\sigma = i\lambda$, with $\lambda^2 < 2k^2$. The issue is of course whether the emergence of discrete modes affect the instability. The answer is no, as we now demonstrate, again focusing on the stronger boundary layer instability.

5.1. *3D extension of the boundary layer instability*

Working with the primitive variables, the appropriate scalings to capture the boundary layer instability are

$$\sigma = -im\Omega(a) + \hat{\sigma}\sqrt{\frac{-m\eta\Omega'(a)}{2a}} + \cdots, \quad \xi := (a-r)\sqrt{\frac{-ma\Omega'(a)}{2\eta}}, \tag{5.7a,b}$$

$$(u, v, w, p) = \left(\sqrt{m\eta}\,\hat{u}, v, \hat{w}\sqrt{\frac{2\Omega(a)}{Z(a)}}, \sqrt{\frac{\eta}{m}}\hat{p}\right) \tag{5.8}$$

in the boundary layer $\xi = O(1)$, where

$$\mu := \frac{k}{m} \tag{5.9}$$

measures the degree of three-dimensionality. With these, the equation set (5.1)–(5.4) reduces to

$$0 = 2\Omega v + \sqrt{-\frac{1}{2}a\Omega'(a)}\frac{\mathrm{d}\hat{p}}{\mathrm{d}\xi}, \tag{5.10}$$

$$\sqrt{\frac{-\Omega'(a)}{2a}}\left(\hat{\sigma} + 2i\xi + \frac{\mathrm{d}}{\mathrm{d}\xi}\right)v = -Z(a)\hat{u} - \frac{i}{a}\hat{p}, \tag{5.11}$$

$$\sqrt{\frac{2\Omega(a)}{Z(a)}}\sqrt{\frac{-\Omega'(a)}{2a}}\left(\hat{\sigma}+2\mathrm{i}\xi+\frac{\mathrm{d}}{\mathrm{d}\xi}\right)\hat{w}=-\mathrm{i}\mu\hat{p}, \tag{5.12}$$

$$-\sqrt{-\frac{1}{2}a\Omega'(a)}\frac{\mathrm{d}\hat{u}}{\mathrm{d}\xi}+\frac{\mathrm{i}v}{a}+\mathrm{i}\mu\sqrt{\frac{2\Omega(a)}{Z(a)}}\hat{w}=0 \tag{5.13}$$

at leading order respectively for small $\sqrt{m\eta}$. Eliminating $\hat{u}$ and $\hat{p}$ then gives

$$\left(\hat{\sigma}+2\mathrm{i}\xi+\frac{\mathrm{d}}{\mathrm{d}\xi}\right)\frac{\mathrm{d}v}{\mathrm{d}\xi}=-\mathrm{i}\gamma\hat{w}, \tag{5.14}$$

$$\left(\hat{\sigma}+2\mathrm{i}\xi+\frac{\mathrm{d}}{\mathrm{d}\xi}\right)\frac{\mathrm{d}\hat{w}}{\mathrm{d}\xi}=\mathrm{i}\gamma v-2\mathrm{i}\hat{w}, \tag{5.15}$$

which is the 3D generalisation of the single boundary layer equation in 2D (see (2.22)), where

$$\gamma:=2a\mu\frac{\sqrt{2(\alpha+2)}}{(-\alpha)}. \tag{5.16}$$

This reduced system only involves m through μ and is valid for $m\ll 1/\eta$. So, for μ held fixed, the growth rate scales with $\sqrt{m}$ (see the rescaling in (5.7)) across the astrophysical regime of $1\ll m\ll 1/\eta$.

In the particular case treated by Ilin & Morgulis (2013) ($\alpha=-2$ so $\gamma=0$) adding an axial wavenumber does nothing to the 2D instability provided ηk stays small. In the general case of interest, $-2\leqslant\alpha<0$ and $\mu>0$ (clearly the stability problem is symmetric under the transformation $(\mu,v,\hat{w})\to(-\mu,v,-\hat{w})$, so only $\mu>0$ needs be considered), a solution is available in terms of Kummer functions. Equations (5.14) and (5.15) can be combined to a single equation for v

$$(\hat{\mathscr{G}}^2+2\mathrm{i}\hat{\mathscr{G}}-\gamma^2)v=0, \tag{5.17}$$

where

$$\hat{\mathscr{G}}:=\frac{\mathrm{d}^2}{\mathrm{d}\xi^2}+(\hat{\sigma}+2\mathrm{i}\xi)\frac{\mathrm{d}}{\mathrm{d}\xi}. \tag{5.18}$$

This can be factored as $(\hat{\mathscr{G}}+4\mathrm{i}\Gamma_1)(\hat{\mathscr{G}}+4\mathrm{i}\Gamma_2)v=0$, where $\Gamma_1:=(1-\sqrt{1-\gamma^2})/4$ and $\Gamma_2:=(1+\sqrt{1-\gamma^2})/4$. Under the change of variable $z:=\mathrm{i}(\hat{\sigma}+2\mathrm{i}\xi)^2/4$, each factor is just Kummer's differential equation,

$$z\frac{\mathrm{d}^2v}{\mathrm{d}\xi^2}+\left(\frac{1}{2}-z\right)\frac{\mathrm{d}v}{\mathrm{d}\xi}-\Gamma_j v=0 \quad j=1,2. \tag{5.19}$$

The solution for v (and therefore indirectly $\hat{w}$) which decays exponentially for $\xi\to\infty$ and $\hat{\sigma}_r>0$ is

$$v=\mathrm{e}^z(\mathscr{A}U(\tfrac{1}{2}-\Gamma_1,\tfrac{1}{2},-z)+\mathscr{B}U(\tfrac{1}{2}-\Gamma_2,\tfrac{1}{2},-z)), \tag{5.20}$$

where U is the multivalued Kummer's function (see NIST 2010, § 13.2.25) and $\mathscr{A}$ and $\mathscr{B}$ are constants. If these are not both to vanish when the further boundary conditions $v=\hat{w}=0$ are imposed at $\xi=0$, then the product

$$U(\tfrac{1}{2}-\Gamma_1,\tfrac{1}{2},-\tfrac{1}{4}\mathrm{i}\hat{\sigma}^2)U(\tfrac{1}{2}-\Gamma_2,\tfrac{1}{2},-\tfrac{1}{4}\mathrm{i}\hat{\sigma}^2)=0, \tag{5.21}$$
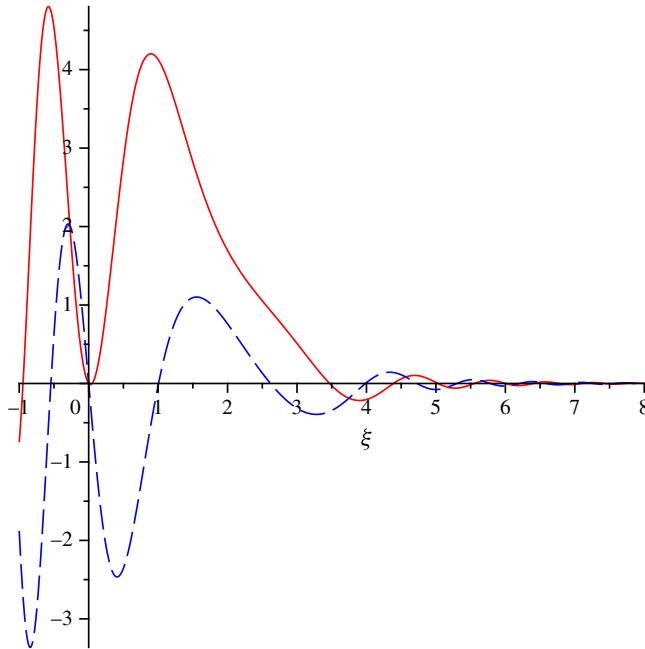
FIGURE 4. (Colour online) The leading growing v eigenfunction calculated using (5.22) in Maple for $m = 1$, $k = 0.3$, $\alpha = -3/2$, corresponding to $\hat{\sigma} = 0.64021 - 4.59526i$ (real/imaginary part is red solid/blue dashed line).

which defines unstable ($\hat{\sigma}_r > 0$) eigenfrequencies $\hat{\sigma}$. The eigenvalues for $\mu > 0$ which smoothly connect with those at $\mu = 0$ are given by $U(1/2 - \Gamma_1, 1/2, -i\hat{\sigma}^2/4) = 0$, since $\mu \to 0$ implies $\Gamma_1 \to 0$ and convergence to the 2D equation $\hat{\mathscr{G}}v = 0$. These eigenfunctions can be plotted using

$$v = \begin{cases} 2\dfrac{\Gamma(\frac{1}{2})}{\Gamma(1 - \Gamma_1)}e^z M\left(\dfrac{1}{2} - \Gamma_1, \dfrac{1}{2}, -z\right) - e^z U\left(\dfrac{1}{2} - \Gamma_1, \dfrac{1}{2}, -z\right) & 0 \leqslant \xi < -\dfrac{1}{2}(\hat{\sigma}_r + \hat{\sigma}_i) \\ e^z U(\frac{1}{2} - \Gamma_1, \frac{1}{2}, -z) & -\frac{1}{2}(\hat{\sigma}_r + \hat{\sigma}_i) \leqslant \xi \end{cases}$$

(5.22)

and $\hat{w} = 2\Gamma_1 v/\gamma$ (with $z := i(\hat{\sigma} + 2i\xi)^2/4$ and '$\Gamma(z)$' indicating the Gamma function), which compensates for the branch cut along the negative real axis in U routinely imposed by packages such as Maple (M is the single-valued Kummer function: § 13.1.2, Abramowitz & Stegun 1964): see figure 4.

Equations (5.14) and (5.15) can also be directly treated numerically (see appendix A). This boundary layer approach works well for the dominant instabilities as μ increases from zero, showing how they are systematically suppressed until their growth rates are comparable to the interior critical layer modes: see figure 5, which shows this for the leading instability. At this point (which is $\mu \approx 0.4$ for $a = 2$, $\eta = 10^{-4}$, $\alpha = -1.5$) the full 3D eigenvalue (5.1)–(5.4) must be solved (see appendix A), which shows the complete suppression of all the instabilities by $\mu = 1$: see figure 6.

The general conclusion is that 3D disturbances are less unstable than 2D disturbances under boundary inflow. In fact, since the boundary layer instability
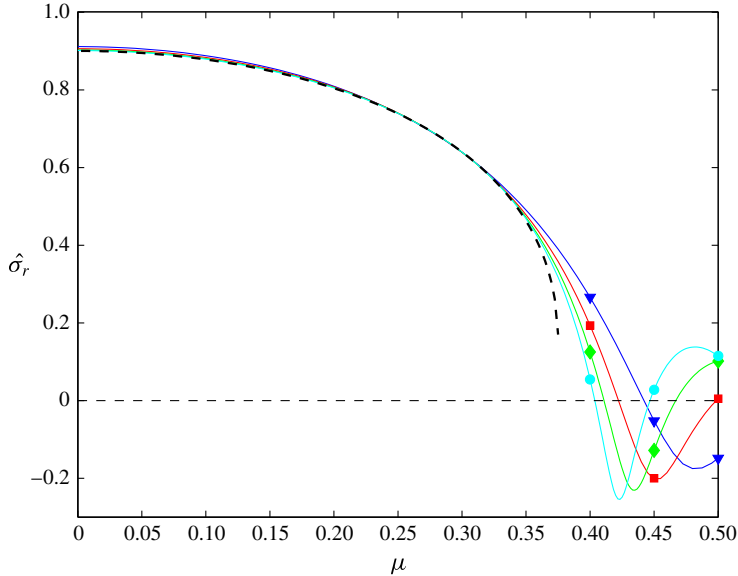
FIGURE 5. (Colour online) Leading inviscid 3D instability for $\alpha = -1.5$, $m = 1$, $a = 2$ with scaled growth rate $\hat{\sigma}_r = \sigma_r / \sqrt{((-m\eta\Omega'(a))/2)/a}$ plotted against μ, the degree of three-dimensionality, as computed using the full eigenvalue code – $\eta = 10^{-4}$ uppermost (blue) line with triangles, $\eta = 10^{-5}$ second uppermost (red) line with squares, $\eta = 10^{-6}$ third uppermost (green) line with diamonds and $\eta = 10^{-7}$ lowest (cyan) line with filled circles – where $N = 1000$ proves sufficient (the markers on each line actually show the $N = 500$ stability results for $\mu = 0.4$, 0.45 and 0.5 to demonstrate convergence). The leading instability is also shown for the boundary layer problem (5.14) and (5.15) as a dashed black line ($N = 4000$). The boundary layer scaling works well, with the full eigenvalue prediction smoothly converging to the boundary layer prediction as $\eta \to 0$ for $\mu \lesssim 0.3$, but beyond this the $\sqrt{\eta}$ scaling is no longer correct. This plot demonstrates that increasing three-dimensionality acts to suppress the 2D instability.

depends only on the shear at the boundary, this could have been anticipated by using a Squires transformation to map a 3D disturbance to a more unstable 2D disturbance (Squires 1933). Normally, such a transformation fails in a rotating system, due to curvature terms, but here these are marginalised by the dispersion relation being only sensitive to the shear at the boundary.

6. Nonlinearity

In this section we examine the nonlinear aspects of the boundary inflow instability. The natural starting point is a weakly nonlinear analysis of the 2D boundary layer instability in the presence of viscosity, so that there is a finite (radial flow) threshold for instability. Then the leading question is whether the new 2D solution branch exists for $\eta \leqslant \eta_{crit}$ (a subcritical bifurcation) or for $\eta \geqslant \eta_{crit}$ (a supercritical bifurcation). This question is most straightforwardly posed with the growing instability not permitted to change the (azimuthally averaged) radial flow, i.e. this is the control parameter of the flow.
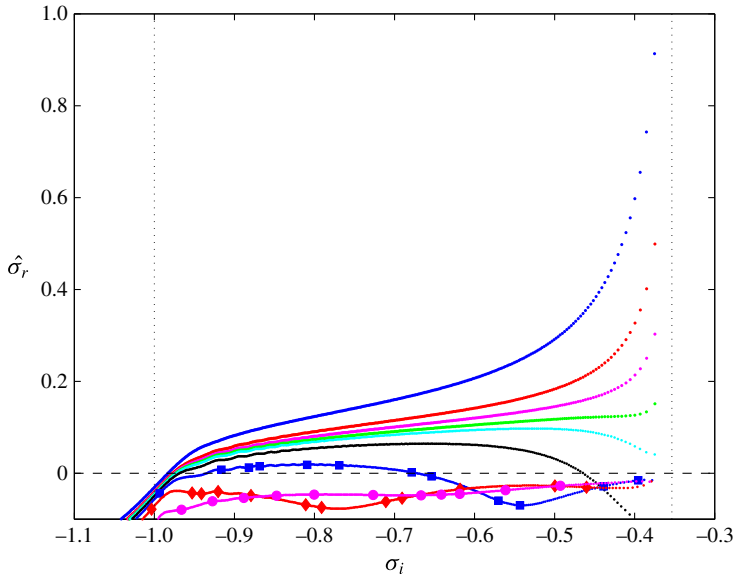
FIGURE 6. (Colour online) Inviscid 3D instabilities for $\alpha = -1.5$, $m = 1$, $a = 2$ and $\eta = 3 \times 10^{-4}$ with scaled growth rate $\hat{\sigma}_r = \sigma_r / \sqrt{-m\eta\Omega'(a)/(2a)}$ plotted against frequency σ_i for various values of μ. The right (left) vertical dashed line is $\sigma_i = -m\Omega(a)$ ($\sigma_i = -m\Omega(1)$). The eigenvalues are calculated from a full 3D eigenvalue calculation with $N = 2400$ for (in order downwards from the uppermost 2D eigenvalues): $\mu = 0$ (blue dots); $\mu = 0.35$ (red dots); $\mu = 0.4$ (magenta dots); $\mu = 0.43$ (green dots); $\mu = 0.45$ (cyan dots); $\mu = 0.5$ (black dots); $\mu = 0.6$ (blue dots with squares); $\mu = 0.75$ (red dots with diamonds) and $\mu = 1$ (magenta dots with circles). This plot demonstrates that increasing three-dimensionality suppresses the 2D instability (in fact completely by $\mu = 0.75$ here). Notice that numerical errors start to creep into the eigenvalues whose eigenfunctions have critical layers far from the inflow boundary (the developing corrugations in the curves) as μ increases (not unexpected as the numerical truncation N is only $O(1/\eta)$).

6.1. *Weakly nonlinear analysis of 2D viscous boundary layer instability*

The analysis revolves almost completely around the boundary layer and can be handled relatively straightforwardly: see appendix B. The growing instability is found to be supercritical, so that the branch of 2D solutions exists for $\eta \geqslant \eta_{crit}$. Along this branch of solutions, the azimuthally averaged radial pressure drop, Δp, across the domain, which is a more natural control parameter for a laboratory experiment, changes. Furthermore, in an accretion disk, maintaining constant angular momentum of the flow is a more natural constraint under which to study flow bifurcations. These, however, just represent different perspectives of viewing the same bifurcation and the ensuing 2D branch of solutions. For example, solutions with constant Δp and varying η are the same as those with constant η and varying Δp, provided the rest of the boundary conditions are consistent (e.g. azimuthally asymmetric radial flow components vanish at the boundaries in both, and the azimuthally asymmetric pressure distribution on each boundary is unconstrained in both). To make this clear and to be able to make statements away from the vicinity of the bifurcation point, we now compute the fully nonlinear 2D solution branch.
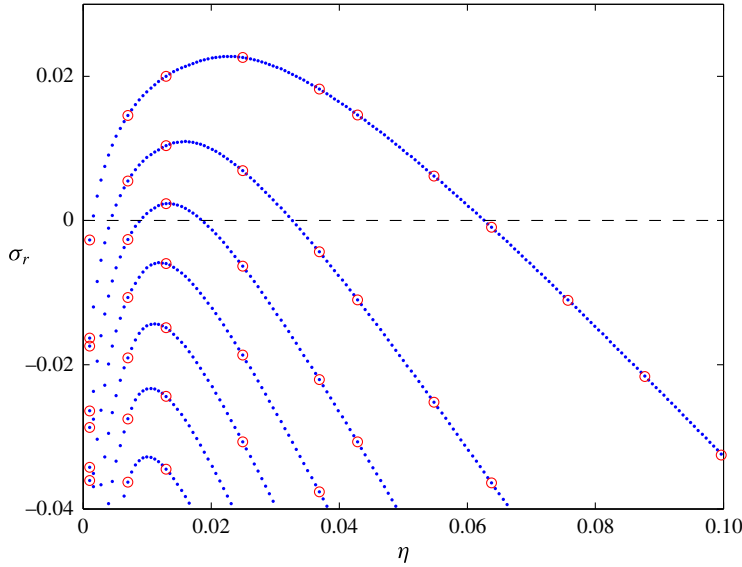
FIGURE 7. (Colour online) The growth rate σ_r versus radial flow η for linear 2D perturbations with $m_0 = 1$ on the 1D basic state (3.1) for $\alpha = -3/2$, $a = 2$ and $Re = 10^5$. The blue dots indicate the eigenvalues using 200 radial modes to represent each component of the perturbation velocity field and the red circles are a sampling of results of using 400 radial modes to confirm convergence. The leading perturbation (top curve) becomes unstable – $\sigma_r > 0$ – at approximately $Re = 5 \times 10^3$ and remains the only instability at $Re = 10^4$.

6.2. *Fully nonlinear 2D solutions*

To study (non-helical) 2D bifurcations off the 1D steady state (3.1), a Reynolds number of $Re = 10^4$ is chosen as a compromise, being hopefully large enough to be in the asymptotic regime but not too large that flows become too arduous to follow numerically. According to the asymptotics, $\eta_{crit} = aN_c^{2/3}\chi^{1/3}Re^{-2/3} \approx 0.0061 \ (0.0087)$ for $m_0 = 1 \ (m_0 = 3)$, whereas actually the thresholds $\eta_{crit} = 0.009635 \ (0.0136)$ are found numerically at $Re = 10^4$ ($\alpha = -3/2$ and $a = 2$). Figure 7 shows how the spectrum of the linear operator depends on η for $Re = 10^5$. Instability is first possible at $Re \approx 5 \times 10^3$ (not shown), with the second mode of instability appearing for $Re > 10^4$, and by $Re = 10^5$ there are three unstable modes. Further computations for $Re = 10^6$ (not shown) show that further modes of instability emerge (now eight) and the persistent feature that each unstable mode is only unstable for a finite range of η. The lower threshold η_l (which is the focus in this work and Gallet *et al.* (2010)) must tend to zero as $Re \to \infty$ to be consistent with the inviscid analysis, whereas the upper threshold η_u must tend to a finite limit to be consistent with the analysis of Ilin & Morgulis (2015a).

The bifurcation is a Hopf bifurcation and the oscillation can be made to look steady by going into a frame rotating at the phase speed $c_\theta := \sigma_i/m_0$ at the bifurcation point. Subsequently, the 2D solution branch is traced out by using the representation

$$\begin{bmatrix} u \\ v \\ p \end{bmatrix} := \sum_{n=0}^{N-1} \sum_{m=0}^{M} \begin{bmatrix} u_{mn}(t)(T_{n+2}(\xi) - T_n(\xi)) \\ v_{mn}(t)(T_{n+2}(\xi) - T_n(\xi)) \\ p_{mn}(t)T_n(\xi) \end{bmatrix} \mathrm{e}^{\mathrm{i}mm_0(\theta - c_\theta t)} + \text{c.c.}, \qquad (6.1)$$
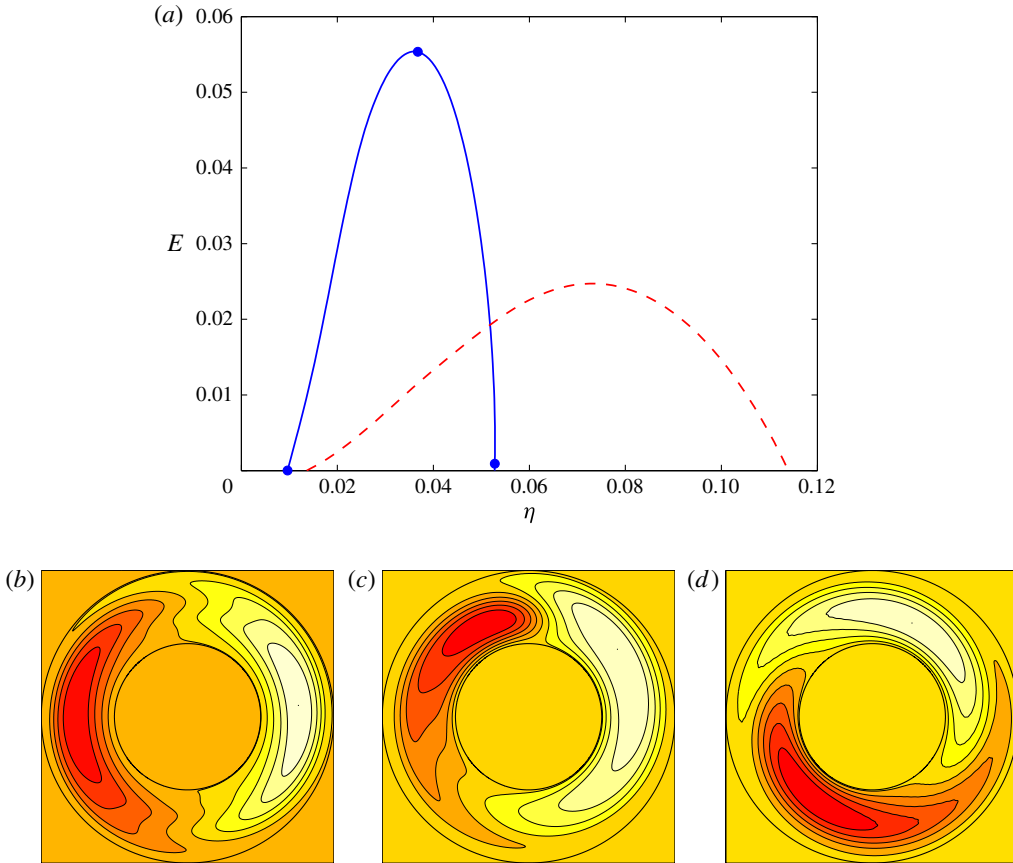
FIGURE 8. (Colour online) (*a*) Kinetic energy per unit length in z of the 2D perturbation, E, versus the radial flow η, with the solid blue line representing the $m_0 = 1$ solution branch and the dashed red line the $m_0 = 3$ branch for $Re = 10^4$, $\alpha = -3/2$ and $a = 2$ (resolution $M = 20$ and $N = 60$). (*b–d*) The 2D stream function for the $m_0 = 1$ solution branch plotted at (*b*) $\eta = 9.64 \times 10^{-3}$, (*c*) 3.67×10^{-2} and (*d*) 5.28×10^{-2} (shown as dots on the solution curve). In each, ten contours are plotted (dark/red-to-light/white being $-$ve to $+$ve); at $\eta = 3.67 \times 10^{-2}$, max $\psi = 0.0478$ and min $\psi = -0.0662$, in all plots, the outer colour/shading indicates the zero contour.

where $T_n(x) := \cos(n \cos^{-1} x)$ are Chebyshev polynomials, $\xi := (2r - a - 1)/(a - 1)$, m_0 indicates the rotational symmetry of the bifurcating eigenfunction and c_θ is the azimuthal phase speed, which is found as part of solution process. Figure 8 shows the new branch of 2D solutions arising from the one unstable mode present at $Re = 10^4$ for $m_0 = 1$ and $m_0 = 3$ found by a Newton–Raphson root-finding algorithm with truncations varying from $(M, N) = (20, 60)$ to $(10, 150)$ (so $O(10^4)$ degrees of freedom). Both bifurcations at the lower threshold η_l are supercritical, consistent with the weakly nonlinear analysis of § 6.1, and the solution branches reconnect with the 1D solution (3.1) at the upper threshold η_u: see figure 8.

Along the 2D solution branch, the 'surplus' azimuthally averaged radial pressure drop,

$$\delta p := (\Delta p)_{2D} - (\Delta p)_{1D} = \int_1^a 2\Omega(r)\bar{v} + \frac{\overline{v^2 - u^2}}{r} \, dr, \qquad (6.2)$$
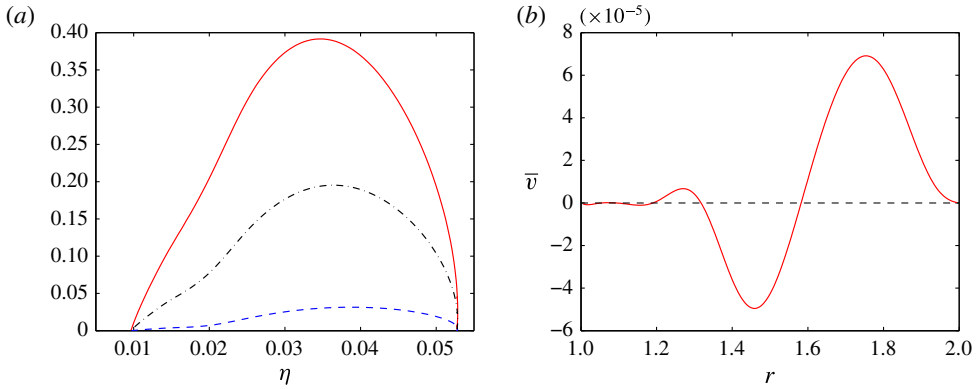
FIGURE 9. (Colour online) (*a*) Surplus azimuthally averaged radial pressure drop δp (blue dashed line), disturbance angular momentum δI (red solid line) and surplus of 2D rotational energy above 1D rotational energy δE (black dash-dot line) all plotted against η for the 2D ($m_0 = 1$) solution branch of figure 8. (*b*) The disturbance angular velocity profile for the 2D ($m_0 = 1$) solution at $\eta = 9.64 \times 10^{-3}$ $Re = 10^4$, $a = 2$ and $\alpha = -3/2$. Notice this closely resembles the prediction of the nonlinear analysis, given that the boundary layer thickness is relatively large ($10^{-4/3}$) and the boundary layer oscillation extends six boundary layer thicknesses outwards.

(where $\overline{(\cdot)} := 1/2\pi \int_0^{2\pi} (\cdot)\, \mathrm{d}\theta$ is just an azimuthal average), the surplus of 2D rotational energy compared to the 1D solution,

$$\delta E := 2\pi \int_1^a (r\Omega\overline{v} + 1/2\overline{v}^2)r\,\mathrm{d}r \qquad (6.3)$$

and the disturbance angular momentum δI are all positive quantities: see figure 9. The initial increase in the pressure drop and the total angular momentum indicates that if either were used as a control parameter instead of the azimuthally averaged radial velocity, the bifurcation would remain supercritical. For example, figure 11 shows a plot of Δp against the azimuthally averaged radial flow parameter η for the 2D solution branch already plotted in figure 8. The weakly nonlinear analysis in appendix B takes η as the control parameter and finds that the bifurcated 2D solution branch exists for $\eta > \eta_{crit}$ (marked as the point A in figure 11) with Δp larger for the 2D solutions than the equivalent (same η) 1D solution (see points B and C in figure 11). If Δp is the control parameter, the bifurcation is still supercritical, as 2D solutions can only exist for $\Delta p \geqslant \Delta p$ at A, but now the bifurcated 2D solutions give rise to two smaller radial inflow solutions (points C or D in figure 11) compared to the 1D solution E.

Another interesting issue for accretion disks is whether this instability acts to transfer angular momentum I outwards. Forming the integral $\int_0^{2\pi} r^2$ (3.4) $\mathrm{d}\theta$ gives the conservation equation

$$\left(\mathscr{I}(r) := \int_0^{2\pi} r[r\Omega(r) + v]r\,\mathrm{d}\theta \right)_t + J_r = 0, \qquad (6.4)$$

where $I = \int_1^a \mathscr{I}(r)\,\mathrm{d}r$ and

$$J := \int_0^{2\pi} \left\{ ruv - \eta v - \frac{1}{Re}r^2\frac{\mathrm{d}}{\mathrm{d}r}\left(\frac{v}{r}\right) \right\} r\,\mathrm{d}\theta \qquad (6.5)$$
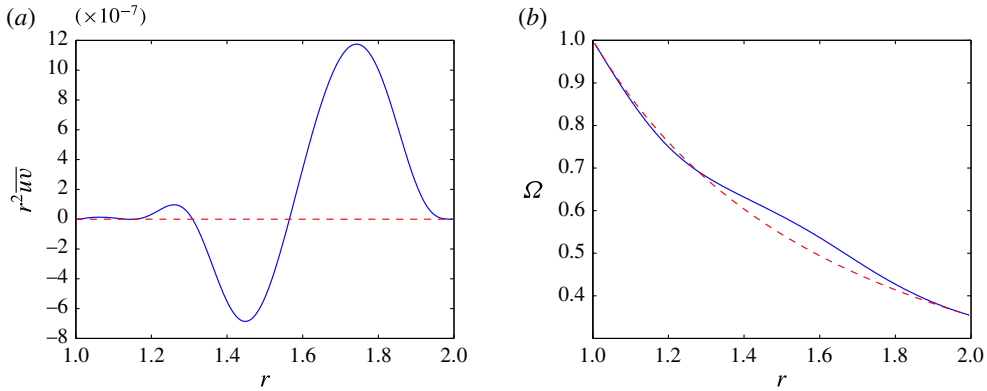
FIGURE 10. (Colour online) (a) $\int_0^{2\pi} r^2 uv \, d\theta$ against r for the bifurcating eigenfunction at $\eta = 9.645 \times 10^{-3}$ (left dot on figure 8(a)). (b) The mean angular velocity profile for the $m_0 = 1$ 2D solution at $\eta = 3.67 \times 10^{-2}$ $Re = 10^4$, $a = 2$ and $\alpha = -3/2$ (solid blue line) and the profile $\Omega = r^\alpha$ corresponding to the 1D basic state (red dashed line). This plot clearly indicates that angular momentum has been transported outwards by the saturated instability.

is the associated radial flux of angular momentum (the flux vanishes for the 1D basic state (3.1)). The first (Reynolds-stress) term in J is computable using the bifurcating eigenfunction alone and can be used to determine the effect of the instability on the angular momentum distribution (the other two terms, which involve nonlinear aspects of the instability, subsequently balance the first term to give a finite amplitude 2D steady state: figure 9(b) actually shows that $r^2\overline{uv} \approx \eta r \overline{v}$). Figure 10 plots this term over the radius for the $m_0 = 1$ state just after the bifurcation (shown in figure 8(a) as the leftmost point at $\eta = 9.645 \times 10^{-3}$) and shows that it alternates in sign but is mostly positive, indicating outwards angular momentum transport. The angular velocity of the 2D state at its maximum amplitude (the middle $m_0 = 1$ point in figure 8(a) and the middle cross-section in figure 8(c)) provides more definitive evidence of this outward transport: see figure 10.

6.3. *Fully nonlinear 3D solutions*

To briefly explore the possibility of 3D states, 3D bifurcations were sought off the 2D branch of $m_0 = 1$ solutions. Concentrating on 3D states with an axial wavenumber $k = 1$, six Hopf bifurcations were found between the initial 2D bifurcation point $\eta = \eta_{2D} = 0.0096$ and $\eta = 0.0152$. These were then traced using the fully nonlinear steady representation

$$\begin{bmatrix} u \\ v \\ w \\ p \end{bmatrix} := \sum_{n=0}^{N-1} \sum_{m=-M}^{M} \sum_{l=0}^{L} \begin{bmatrix} u_{lmn}(t)(T_{n+2}(\xi) - T_n(\xi)) \\ v_{lmn}(t)(T_{n+2}(\xi) - T_n(\xi)) \\ w_{lmn}(t)(T_{n+2}(\xi) - T_n(\xi)) \\ p_{lmn}(t)T_n(\xi) \end{bmatrix} e^{i(mm_0\theta^* + lkz^*)} + \text{c.c.} \quad (6.6)$$

by moving into a frame moving with the phase speed c_z in z (initially $c_z := \sigma_i/k$ at the bifurcation point, where σ_i is the instability frequency). Since $\theta^* := \theta - c_\theta t$ already incorporates the phase speed of the initial 2D instability, these secondary 3D states are steady in a rotating and translating frame. Figure 12 shows that all the traced
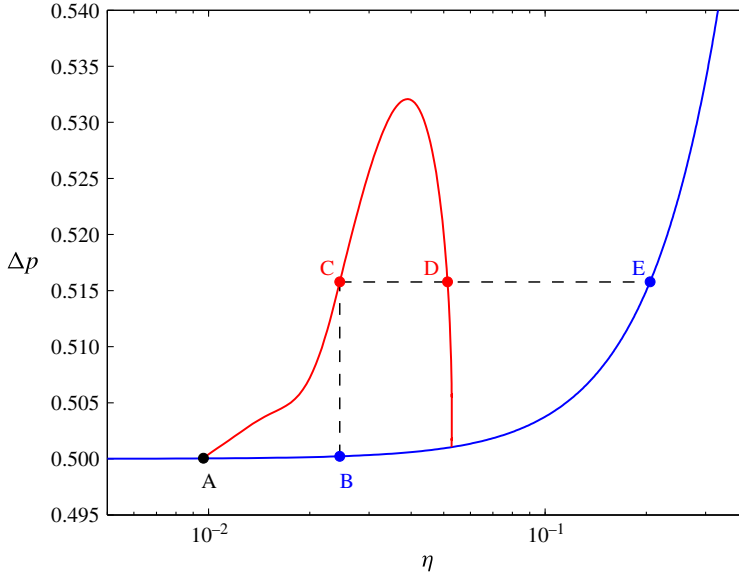
FIGURE 11. (Colour online) The azimuthally averaged radial pressure drop Δp is plotted again the azimuthally averaged radial flow η for the undisturbed 1D basic state (blue solid line connecting points A, B and E; $\Delta p_{1D} := (1 - 1/a) + (\eta^2(1 - 1/a^2))/2)$ and the 2D solutions (red solid line connecting points A, C and D) which emanate out of the bifurcation for $m_0 = 1$, $a = 2$, $Re = 10^4$ and $\alpha = -3/2$ (as shown in figure 8). The bifurcation point is point A, and the plot shows that the bifurcation is supercritical for either η or Δp being the control parameter. Note that, if Δp is fixed, the bifurcation leads to states with lower radial flow (compare states C and D with E).

bifurcations are supercritical, i.e. there is no evidence of solution branches reaching $\eta < \eta_{2D}$. Solution branches are shown as far as they are reproducible using different truncation levels. The maximum realistic resolution was $(N, M, L) = (40, 20, 4)$, giving 58 963 degrees of freedom, since the branch continuation approach was a direct Newton–Raphson solver, albeit with multithreaded linear algebra software. A typical 3D flow is shown in figure 13, with the presence of vertical jets at the outflow boundary and the lack of any large-scale structure being particularly noteworthy.

7. Energetics

The instability is inviscid in nature, so we first consider the energetics of this simplest situation: note that in the absence of viscosity, $\alpha = -2$ gives the only consistent solution. If $\boldsymbol{u}_{tot} = \boldsymbol{U} + \boldsymbol{u}$ is the total velocity field, then the scalar product of this with the governing Euler equations gives

$$\partial_t \left\langle \frac{1}{2}\boldsymbol{u}_{tot}^2 \right\rangle = - \oint \frac{1}{2}\boldsymbol{u}_{tot}^2(\boldsymbol{u}_{tot} \cdot \mathrm{d}S) - \oint p\boldsymbol{u}_{tot} \cdot \mathrm{d}S. \quad (7.1)$$

With no disturbance $\boldsymbol{u} = 0$, this amounts to

$$- \oint p\boldsymbol{u}_{tot} \cdot \mathrm{d}S = \eta \int_0^{2\pi} \mathrm{d}\theta \int \mathrm{d}z[p(a, \theta, z, t) - p(1, \theta, z, t)] = \pi\eta(1 + \eta^2)\left(1 - \frac{1}{a^2}\right) \quad (7.2)$$
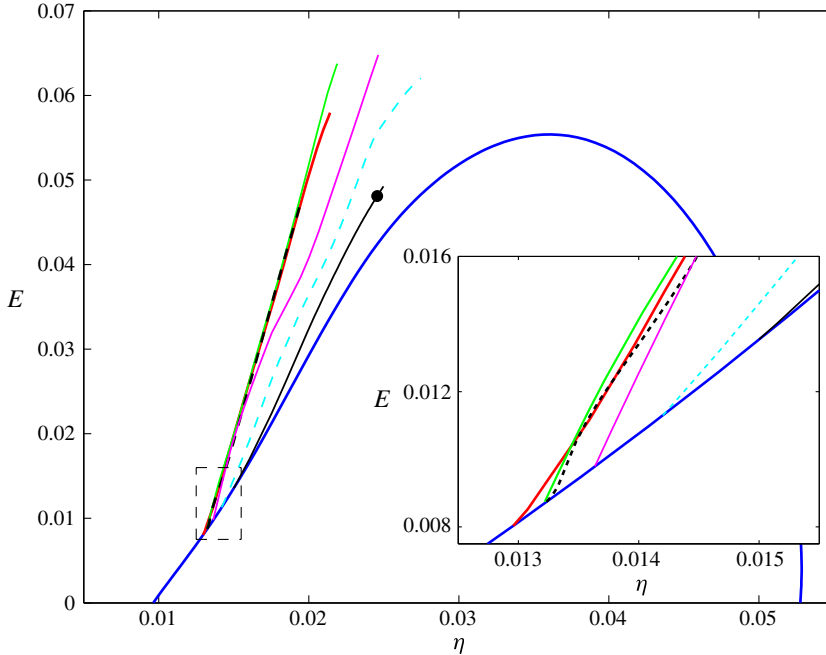
FIGURE 12. (Colour online) The 3D solution branches continued out of the six Hopf bifurcations (see the inset, which magnifies the dashed box for detail) from the 2D branch (thick blue loop as in figure 8) found for $m_0 = 1$ at $Re = 10^4$, $\alpha = -3/2$, $k = 1$ and $a = 2$. All the bifurcations are supercritical. The ordinate is the disturbance energy (2D and 3D) and the abscissa the radial flow η. The black dot indicates the particular 3D flow state shown in detail in figure 13. Typically a resolution of $(N, M, L) = (40, 20, 4)$ was used to follow these solutions, with curve segments only shown if they are robust under truncation changes.

so a net pressure drop radially inwards across the domain drives the radial flow and works at a rate to replenish the net kinetic energy, leaving the domain (the rightmost term using $\boldsymbol{U} = -\eta/r\hat{\boldsymbol{r}} + 1/r\hat{\boldsymbol{\theta}}$).

The need for interior shear to fuel the instability is apparent by looking at the disturbance energy balance. Taking the scalar product of the disturbance velocity $\boldsymbol{u}$ and the disturbance evolution equation, leads to

$$\frac{\mathrm{d}}{\mathrm{d}t} \left\langle \frac{1}{2}\boldsymbol{u}^2 \right\rangle = -\langle \boldsymbol{u} \cdot \boldsymbol{\nabla U} \cdot \boldsymbol{u} \rangle - \eta \int_0^{2\pi} \frac{1}{2}v^2 \bigg|_{r=1} \mathrm{d}\theta, \qquad (7.3)$$

or explicitly

$$\frac{\mathrm{d}}{\mathrm{d}t} \left\langle \frac{1}{2}\boldsymbol{u}^2 \right\rangle = \eta \left\langle \frac{v^2 - u^2}{r^2} \right\rangle - \left\langle ruv\frac{\mathrm{d}\Omega}{\mathrm{d}r} \right\rangle - \eta \int_0^{2\pi} \frac{1}{2}v^2 \bigg|_{r=1} \mathrm{d}\theta, \qquad (7.4)$$

so the disturbance can only gain energy through the underlying shear field (the last term on the right-hand side is the loss of kinetic energy through the outflow boundary). The second term on the right-hand side is the energy transfer from the swirl field, and this has to be positive (i.e. the underlying swirl field supplies energy to the disturbance) for a growing disturbance to achieve growth rates $\gg O(\eta)$.
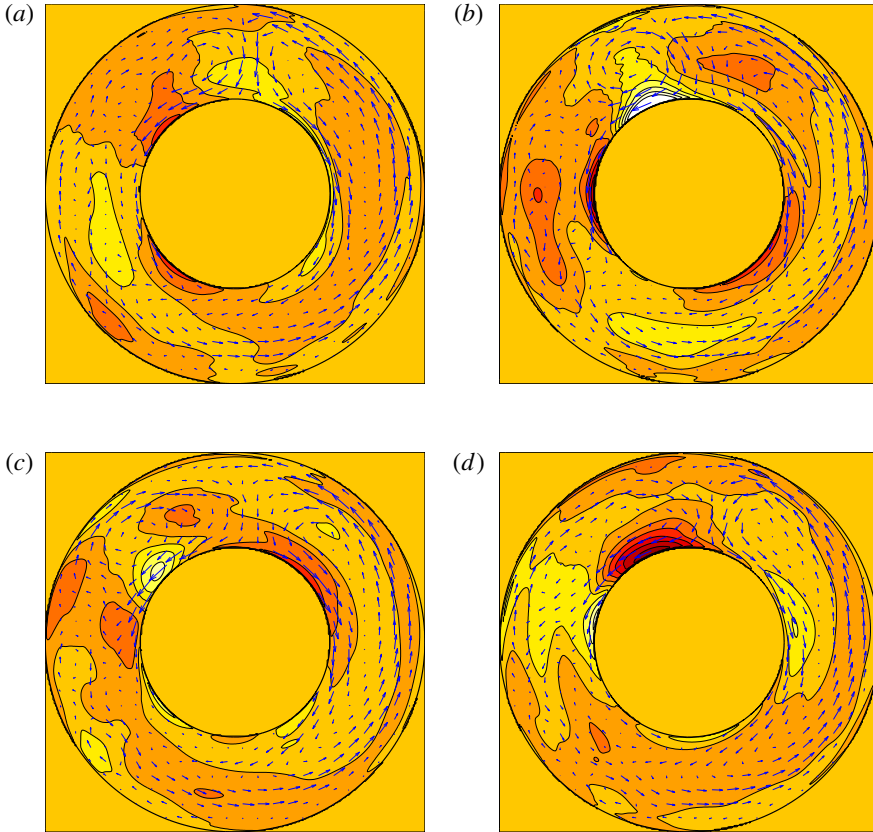
FIGURE 13. (Colour online) A typical 3D state (shown as a dot on figure 12) calculated using $(N, M, L) = (40, 28, 4)$ (82 003 degrees of freedom) plotted at $z = 0$ (a), $z = \pi/2$ (b), $z = \pi$ (c) and $z = 3\pi/2$ (d) (axial wavelength $= 2\pi$). The axial speed is shown by 10 contours going from -0.025 to 0.035 (the colour/shading of the zero contour is shown on the outside of the flow domain). The arrows indicate the speed and direction of the flow in the (r, θ) plane, with the longest arrow representing a speed of 0.272.

Adding viscosity complicates the (energetic) situation by introducing interior dissipation and the further possibility of viscous stresses at either or both radial boundaries inputting energy into the flow: explicitly

$$\frac{\mathrm{d}}{\mathrm{d}t} \left\langle \frac{1}{2} \boldsymbol{u}_{tot}^2 \right\rangle = \eta \int_0^{2\pi} \mathrm{d}\theta \int \mathrm{d}z \left[\frac{1}{2} \boldsymbol{u}_{tot}^2(a, \theta, z, t) - \frac{1}{2} \boldsymbol{u}_{tot}^2(1, \theta, z, t) \right.$$

$$\left. + p_{tot}(a, \theta, z, t) - p_{tot}(1, \theta, z, t) \right]$$

$$+ \frac{1}{Re} \oint \boldsymbol{u}_{tot} \cdot 2\boldsymbol{e} \cdot \mathrm{dS} - \frac{1}{Re} \langle 2\boldsymbol{e} : \boldsymbol{e} \rangle, \tag{7.5}$$

where $\boldsymbol{e}$ is the rate of strain tensor for $\boldsymbol{u}_{tot}$. However, non-slip boundary conditions and constant η do at least fix the net advection of kinetic energy out of the domain. Then either an increased radial pressure drop and/or increased work done by viscous stresses at the walls must offset the greater dissipation of a 2D bifurcated state. Certainly the

nonlinear computations of §6 suggest that the radial pressure drop does go up for the bifurcated solutions. For an accretion disk, however, it may be more realistic to assume that the radial pressure drop is fixed but the radial flow η can change instead. In this case, rather paradoxically, figure 11 indicates that the 2D flow will adopt a smaller radial flow to accommodate the greater dissipation of the 2D state. This runs counter to the usual argument that a turbulent disk should set up, via an enhanced eddy viscosity, a more accreting flow travelling down the gravitational potential to power it.

8. Discussion

In this paper we have revisited the 2D instability discussed separately by Nicoud & Angilella (1997), Doering *et al.* (2000), Gallet *et al.* (2010) and Ilin & Morgulis (2013) in various contexts to explore the interesting mathematical and physical issues surrounding it. A simple half-plane model indicates that the instability operates by the cross-flow advecting vorticity introduced by the inflow boundary across the cross-stream shear. Imposing vanishing vorticity at the inflow boundary eliminates the instability. This half-plane model also makes it clear that curvature or rotation is not important, other than to restrict the allowed streamwise wavenumbers (azimuthal periodicity prevents very long wavelengths, which are the most unstable in the rectilinear situation). It also highlights the fact that only inflow is destabilising, suggesting that, in situations where there is both an inflow and an outflow, the inflow boundary could be expected to destabilise the flow initially as the cross-flow is turned on before the outflow (or 'suction') boundary eventually stabilises the flow at a higher cross-flow value. This is clearly seen in circumstances where the underlying shear flow is not modified by the cross-flow (e.g. Nicoud & Angilella 1997; Ilin & Morgulis 2013; and here in §2) but seems generally true even if it does (e.g. Doering *et al.* 2000; Fransson & Alfredsson 2003; Gallet *et al.* 2010; Guha & Frigaard 2010; Deguchi *et al.* 2014; Ilin & Morgulis 2015*a*, although note Hains 1971). The identification of the instability with inflow also explains why this instability is relatively unstudied compared to outflow boundaries, long lauded as a reliable means to stabilise unidirectional flows (e.g. Joslin 1998).

One of the most interesting aspects of this 'boundary inflow instability' is that the growth rates scale as $\sqrt{\eta}$ for boundary layer modes and $\eta \log 1/\eta$ for interior critical layer modes when the perturbing cross-flow is only $O(\eta)$. This means that the instability has to draw energy out of the underlying shear field. However, the 2D nonlinear solutions computed in the rotating situation do not show any despinning of the swirl field, but instead indicate that the radial pressure gradient which drives the cross-flow more than replenishes this energy by working on the flow.

The apparently delicate mathematical structure underlying the instability – the lack of any discrete normal modes for the inviscid, vanishing cross-flow situation – suggests that additional physics may easily suppress it. However, the work by Gallet *et al.* (2010) already indicated that it could survive the addition of viscosity (see also Ilin & Morgulis 2015*a*) and here we have also explored different (more Rayleigh-stable) rotation profiles plus the addition of three-dimensionality (see also Ilin & Morgulis 2015*b*) and compressibility. It is true that, except for the rotation profiles, none of these have actually enhanced the instability (e.g. 2D modes are more unstable than 3D modes), but neither have they immediately suppressed it either (e.g. the viscous threshold for the instability is still only a very small cross-flow of $O(Re^{-1})$ in a rectilinear geometry (Nicoud & Angilella 1997) and $O(Re^{-2/3})$ in the rotating

situation; see § 3.4). The conclusion is therefore that the instability is relatively robust, except to the exact boundary conditions imposed at the inflow boundary, and one should therefore expect instability whenever there is boundary inflow together with shear.

Weakly nonlinear analysis of the primary bifurcation and branch continuation of the fully nonlinear 2D solutions indicate that the instability is supercritical in the cross-flow. Furthermore, secondary bifurcations to 3D states also appear supercritical (six were found and continued) suggesting a succession of bifurcations in which the flow gradually becomes more complicated spatially and temporally as the cross-flow is increased. This all makes the boundary inflow instability an inviting target for an experimental study, especially as the primary instability is oscillatory and hence clearly identifiable.

Astrophysically, we have established that a Keplerian rotation profile with cross-flow of $-\eta/r\hat{r}$ and non-slip boundary conditions at the inflow boundary will be unstable if the cross-flow $\eta \gtrsim O(Re^{-2/3})$ – hence Rayleigh's stability criterion can be circumvented by cross-flow. However, in a quiescent disk, (molecular) viscous stresses only generate a cross-flow of $O(Re^{-1})$, so the linear instability is not triggered. Moreover, both the (2D) primary and (3D) secondary instabilities are supercritical, so there is also no apparent opportunity to reach the instability via finite amplitude perturbations at such low cross-flows. Even if the cross-flow were large enough, one would have to argue that the appropriate boundary conditions were in place at the inflow (outer) boundary of the disk. Nevertheless, the analysis presented here does highlight the potential for mass entering a disk to disrupt the orbiting flow if this mass flux possesses vorticity, and also showcases the complications of introducing inflow boundaries in disk models (e.g. Kersale *et al.* 2004).

Acknowledgement

Appendix A. Numerics

The 3D boundary layer equations (5.14) and (5.15) can be directly treated numerically by transforming the domain $\xi \in [0, \infty)$ to $x \in [-1, 1)$ via the definition $x := (\xi - L)/(\xi + L)$, where L is a scale factor ($L = 1$ works well here). v and $\hat{w}$ are expanded as differences of consecutive even or odd Chebyshev polynomials

$$(v, \hat{w}) = \sum_{n=0}^{N} (a_n, b_n)(T_{n+2}(X) - T_n(X)), \quad \text{where } T_n(x) := \cos(n \cos^{-1} x) \qquad (A\,1)$$

so that v and $\hat{w}$ are forced to vanish at $\xi = 0$ and $\xi \rightarrow \infty$, and the two equations (5.14) and (5.15) are collocated across the N zeros of $T_N(X)$. The resulting $2N \times 2N$ eigenvalue problem (with N varying from 100 to 10 000) is then solved using LAPACK routine ZGGEV (solving the 2D boundary layer equation (2.22) is just a $N \times N$ special case of the 3D problem). The viscous boundary layer equation (3.44) can be similarly solved.

The full 3D eigenvalue (5.1)–(5.4) can be solved by expanding the primitive variables as follows

$$\left[u, \begin{pmatrix} v \\ w \end{pmatrix}, p \right] := \sum_{n=0}^{N} \left[a_n(T_{n+2}(Y) - T_n(Y)), \begin{pmatrix} b_n \\ c_n \end{pmatrix} (T_{n+1}(Y) - T_n(Y)), d_n T_n(Y) \right], \quad (A\,2)$$

where $Y := (2r - a - 1)/(a - 1)$ so that the appropriate boundary conditions – $u = 0|_{r=1}$, $u = v = w|_{r=a} = 0$ – are automatically imposed. This $4N \times 4N$ eigenvalue problem is again solved by LAPACK routine ZGGEV typically, with $N = 2400$. An associated inverse iteration code was developed where N could reach $12\,000$ on a 128 GB machine to confirm eigenvalues.

Appendix B. Weakly nonlinear analysis of 2D viscous boundary layer instability

We introduce two small quantities: δ as the amplitude of the instability and $\epsilon = Re^{-1/3}$ as a measure of the viscosity. The analysis proceeds from the following expansion of the velocity field

$$
\begin{aligned}
\psi = {}& \delta\{(\psi_{10}^{(m)}(r) + \hat{\psi}_{10}^{(m)}(y)) + \epsilon(\psi_{11}^{(m)}(r) + \hat{\psi}_{11}^{(m)}(y)) + \cdots\}E(\theta, t) \\
&+ \delta\left(\frac{\delta}{\epsilon^2}\right)\left(\frac{m}{a}\right)\left\{\frac{1}{\epsilon}\psi_{2,-1}^{(0)}(r) + N_c^{1/3}\chi^{-1/3}(\psi_{20}^{(0)}(r) + \hat{\psi}_{20}^{(0)}(y)) + O(\epsilon))\right\} \\
&+ \delta\left(\frac{\delta}{\epsilon^2}\right)\left(\frac{m}{a}\right)N_c^{1/3}\chi^{-1/3}\{(\psi_{20}^{(2m)}(r) + \hat{\psi}_{20}^{(2m)}(y)) + O(\epsilon)\}E(\theta, t)^2 \\
&+ \delta\left(\frac{\delta}{\epsilon^2}\right)^2\left(\frac{m}{a}\right)^2 N_c^{2/3}\chi^{-2/3}\{(\psi_{30}^{(m)}(r) + \hat{\psi}_{30}^{(m)}(y)) + O(\epsilon)\}E(\theta, t) \\
&+ \delta\left(\frac{\delta}{\epsilon^2}\right)^2\left(\frac{m}{a}\right)^2 N_c^{2/3}\chi^{-2/3}\{(\psi_{30}^{(3m)}(r) + \hat{\psi}_{30}^{(3m)}(y)) + O(\epsilon)\}E(\theta, t)^3 \\
&+ \cdots + \text{c.c.},
\end{aligned} \tag{B 1}
$$

where

$$
E(\theta, t) := e^{im\theta + (-im\Omega(a) + \epsilon\hat{\sigma})t}, \tag{B 2}
$$

$$
y := N_c^{-1/3}\chi^{1/3}\left(\frac{a - r}{\epsilon}\right), \tag{B 3}
$$

$$
\hat{\sigma} := N_c^{1/3}\chi^{2/3}\hat{\sigma}_0 + \left(\frac{\delta}{\epsilon^2}\right)^2\left(\frac{m}{a}\right)^2\hat{\sigma}_2 + \cdots, \tag{B 4}
$$

$$
\eta := \epsilon^2\hat{\eta}_c + \epsilon^2\left(\frac{\delta}{\epsilon^2}\right)^2\frac{m^2}{a}N_c^{1/3}\chi^{-1/3}\hat{\eta}_2 + \cdots, \tag{B 5}
$$

with $N_c = 4.57557$, $\hat{\sigma}_0 = -5.63551i$ and $\hat{\eta}_c = aN_c^{2/3}\chi^{1/3}$ being the critical values (see § 3.4) and $\chi = -m\Omega'(a)/2$ (only the flow components $\hat{\psi}_{10}^{(m)}(y)$, $\hat{\psi}_{20}^{(0)}(y)$ and $\hat{\psi}_{20}^{(2m)}(y)$ need to be calculated). The objective here is to look around the bifurcation point $\eta = \epsilon^2\hat{\eta}_c$, where $\delta = 0$ (fixed Re), to find a value of $\hat{\eta}_2$ consistent with $\delta > 0$: $\hat{\eta}_2 < 0(>0)$ indicates a subcritical (supercritical) bifurcation. We work with the full 2D disturbance equation (3.8)

$$
\left(\frac{\partial}{\partial t} + \Omega(r)\frac{\partial}{\partial\theta} - \frac{\eta}{r}\frac{\partial}{\partial r}\right)\Delta\psi = \frac{1}{r}\frac{dZ}{dr}\frac{\partial\psi}{\partial\theta} + \frac{1}{Re}\Delta^2\psi + \frac{1}{r}J(\psi, \Delta\psi). \tag{B 6}
$$

B.1. *Linear problem at $O(\delta)$*

The boundary layer problem is fourth order in y

$$
\left[\frac{d^2}{dy^2} - N_c\frac{d}{dy} - N_c(\hat{\sigma}_0 + 2iy)\right]\frac{d^2\hat{\psi}_{10}^{(m)}}{dy^2} = 0, \tag{B 7}
$$

with the boundary conditions that $\hat{\psi}_{10}^{(m)}$, $\mathrm{d}\hat{\psi}_{10}^{(m)}/\mathrm{d}y$ and $\mathrm{d}^2\hat{\psi}_{10}^{(m)}/\mathrm{d}y^2$ all vanish at large y and $\mathrm{d}\hat{\psi}_{10}^{(m)}/\mathrm{d}y = 0$ at $y = 0$. The outer (leading order) problem is second order in r

$$[\Omega(r) - \Omega(a)]\mathscr{L}\psi_{10}^{(m)} = \frac{1}{r}\frac{\mathrm{d}Z}{\mathrm{d}r}\psi_{10}^{(m)} \tag{B 8}$$

($m \neq 0$), to which the appropriate boundary conditions are $\psi_{10}^{(m)}(1) = 0$ ($u(1) = 0$) and $\psi_{10}^{(m)}(a) = -\hat{\psi}_{10}^{(m)}$, so $u(a) = 0$. (Formally there is a weak viscous layer at $r = 1$ of thickness $O(1/Re)$ where the stream function boundary correction is $O(1/Re)$ to accommodate the non-slip condition $v(1) = 0$, but this plays no role in the nonlinear equilibration of the instability centred on the other boundary and will be ignored here and below.) The boundary layer problem alone identifies the bifurcation point (see §3.4).

B.2. *Nonlinearity* $O(\delta(\delta/\epsilon^2))$

Nonlinearity comes in at $O(\delta(\delta/\epsilon^2))$, generating boundary flows $\hat{\psi}_{20}^{(0)}$ and $\hat{\psi}_{20}^{(2m)}$ as follows. For $\hat{\psi}_{20}^{(0)}$

$$\left[\frac{\mathrm{d}^4}{\mathrm{d}y^4} - N_c\frac{\mathrm{d}^3}{\mathrm{d}y^3}\right]\hat{\psi}_{20}^{(0)} = -\mathrm{i}\left\{(\hat{\psi}_{10}^{(m)} + \psi_{10}^{(m)})\frac{\mathrm{d}^3\hat{\psi}_{10}^{*(m)}}{\mathrm{d}y^3} + \frac{\mathrm{d}\hat{\psi}_{10}^{(m)}}{\mathrm{d}y}\frac{\mathrm{d}^2\hat{\psi}_{10}^{*(m)}}{\mathrm{d}y^2}\right\} + \text{c.c.,} \tag{B 9}$$

where the solution which vanishes as $y \to \infty$ is sought. In the boundary layer, the outer solution $\psi_{10}^{(m)}$ is just the constant $-\hat{\psi}_{10}^{(m)}(0)$ and, since $\mathrm{Re}(\mathrm{i}|\mathrm{d}\hat{\psi}_{10}^{(m)}/\mathrm{d}y|^2) = 0$, (B 9) can be integrated twice to give

$$\left[\frac{\mathrm{d}^2}{\mathrm{d}y^2} - N_c\frac{\mathrm{d}}{\mathrm{d}y}\right]\hat{\psi}_{20}^{(0)} = f_0(y) := 2\,\mathrm{Re}\left\{-\mathrm{i}(\hat{\psi}_{10}^{(m)}(y) - \hat{\psi}_{10}^{(m)}(0))\frac{\mathrm{d}\hat{\psi}_{10}^{*(m)}}{\mathrm{d}y}\right\} \tag{B 10}$$

and the required boundary layer solution is

$$\hat{\psi}_{20}^{(0)}(y) = \int_y^\infty \frac{1 - \mathrm{e}^{N_c(y-x)}}{N_c}f_0(x)\,\mathrm{d}x. \tag{B 11}$$

This cannot be made to satisfy the no-slip condition $\mathrm{d}\hat{\psi}_{20}^{(0)}/\mathrm{d}y = 0$ at $y = 0$, and so drives an interior mean flow $\psi_{2,-1}^{(0)}$ via

$$\left.\frac{\mathrm{d}\psi_{2,-1}^{(0)}}{\mathrm{d}r}\right|_{r=a} - \left.\frac{\mathrm{d}\hat{\psi}_{20}^{(0)}}{\mathrm{d}y}\right|_{y=0} = 0, \tag{B 12}$$

to ensure $v = 0$ at $r = a$. The interior mean flow problem for $\psi_{2,-1}^{(0)}$ is just

$$\frac{\mathrm{d}}{\mathrm{d}r}\left(\frac{\mathrm{d}}{\mathrm{d}r} + \frac{1}{r}\right)\frac{\mathrm{d}\psi_{2,-1}^{(0)}}{\mathrm{d}r} = 0, \tag{B 13}$$

with boundary conditions $\quad \left.\frac{\mathrm{d}\psi_{2,-1}^{(0)}}{\mathrm{d}r}\right|_{r=1} = 0, \quad \left.\frac{\mathrm{d}\psi_{2,-1}^{(0)}}{\mathrm{d}r}\right|_{r=a} = -\int_0^\infty \mathrm{e}^{-N_c x}f_0(x)\,\mathrm{d}x,$
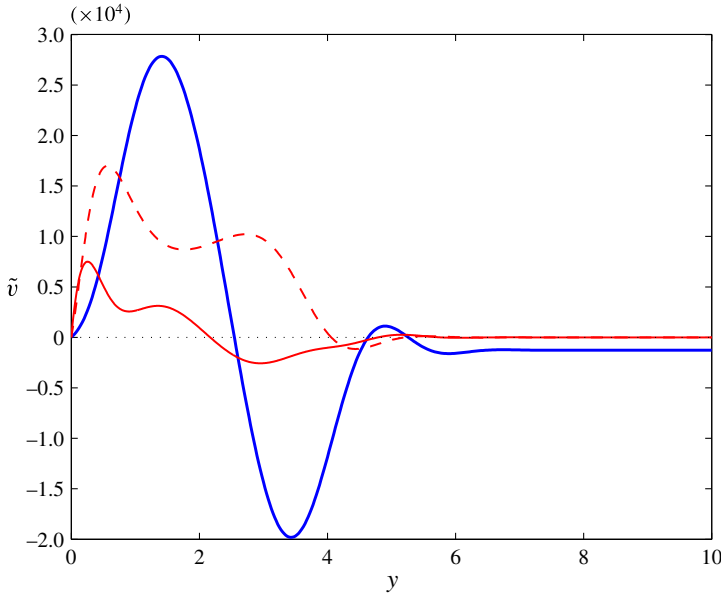
$$\tag{B 14}$$

FIGURE 14. (Colour online) Azimuthal velocities for the (scaled) boundary layer mean flow at $O(m\delta^2/a\epsilon^3)$: $\tilde{v} := (\mathrm{d}\hat{\psi}_{20}^{(0)}/\mathrm{d}y - \mathrm{d}\psi_{2,-1}^{(0)}/\mathrm{d}r|_{r=a})$ (thick solid blue line) and the second harmonic $- \mathrm{d}\hat{\psi}_{20}^{(2m)}/\mathrm{d}y$ (real/imaginary part solid/dashed red line) – plotted against y, the boundary layer variable.

since the leading interior nonlinear term $J(\psi_{10}^{(m)}, \Delta\psi_{10}^{*(m)}) + \text{c.c.}$ only drives a mean flow at an $O(\epsilon)$ smaller level. The solution is

$$\frac{\mathrm{d}\psi_{2,-1}^{(0)}}{\mathrm{d}r} = -2\frac{a(r^2-1)}{r(a^2-1)}\int_0^\infty \mathrm{e}^{-N_c x} f_0(x)\,\mathrm{d}x \approx 2539\frac{a(r^2-1)}{r(a^2-1)}, \tag{B 15}$$

so the mean flow $(\propto -\mathrm{d}\psi_{2,-1}^{(0)}/\mathrm{d}r)$ is a decreasing function of the radius until the boundary layer is reached. There the mean flow undergoes an oscillation, finally increasing sharply close to the boundary: see figure 14.

For $\hat{\psi}_{20}^{(2m)}$,

$$\left[\frac{\mathrm{d}^2}{\mathrm{d}y^2} - N_c\frac{\mathrm{d}}{\mathrm{d}y} - 2N_c(\hat{\sigma}_0 + 2\mathrm{i}y)\right]\frac{\mathrm{d}^2\hat{\psi}_{20}^{(2m)}}{\mathrm{d}y^2}$$
$$= \frac{\mathrm{d}}{\mathrm{d}y}\left[-\mathrm{i}\left(\frac{\mathrm{d}\hat{\psi}_{10}^{(m)}}{\mathrm{d}y}\right)^2 + \mathrm{i}(\hat{\psi}_{10}^m(y) - \hat{\psi}_{10}^m(0))\frac{\mathrm{d}^2\hat{\psi}_{10}^{(m)}}{\mathrm{d}y^2}\right]. \tag{B 16}$$

A particular integral for $\mathrm{d}^2\hat{\psi}_{20}^{(2m)}/\mathrm{d}y^2$ can be generated by the variation of parameters method given that the complementary problem,

$$\left[\frac{\mathrm{d}^2}{\mathrm{d}y^2} - 2\alpha\frac{\mathrm{d}}{\mathrm{d}y} - (\beta\gamma^2 - \alpha^2 + \gamma^3 y)\right]\frac{\mathrm{d}^2\hat{\psi}_{20}^{(2m)}}{\mathrm{d}y^2} = 0, \tag{B 17}$$

has solutions $\mathrm{e}^{\alpha y}\mathrm{Ai}(\beta + \gamma y)$ and $\mathrm{e}^{\alpha y}\mathrm{Bi}(\beta + \gamma y)$, but the ensuing integral expressions become unwieldy when integrated twice to get $\hat{\psi}_{20}^{(2m)}$, which is needed below. Instead, it is better to numerical solve (B 16) directly. In fact (B 16) can be integrated once to

$$
\left[\frac{\mathrm{d}^3}{\mathrm{d}y^3} - N_c \frac{\mathrm{d}^2}{\mathrm{d}y^2} - 2N_c(\hat{\sigma}_0 + 2\mathrm{i}y)\frac{\mathrm{d}}{\mathrm{d}y} + 4\mathrm{i}N \right] \hat{\psi}_{20}^{(2m)}
$$
$$
= f_2(y) := -\mathrm{i}\left(\frac{\mathrm{d}\hat{\psi}_{10}^{(m)}}{\mathrm{d}y} \right)^2 + \mathrm{i}(\hat{\psi}_{10}^m(y) - \hat{\psi}_{10}^m(0))\frac{\mathrm{d}^2\hat{\psi}_{10}^{(m)}}{\mathrm{d}y^2}, \tag{B 18}
$$

where a vanishing solution is sought as $y \to \infty$. The (numerical) solution strategy is to actually work over the domain $y \in [0, y_{max}]$ (with y_{max} 'large' but finite), which is transformed to $x \in [-1, 1]$ by the definition $x := 2y/y_{max} - 1$, and to expand $\mathrm{d}\hat{\psi}_{20}^{(2m)}/\mathrm{d}y$ as

$$
\frac{\mathrm{d}\hat{\psi}_{20}^{(2m)}}{\mathrm{d}y} = \sum_{n=0}^{N} a_n(T_{n+2}(x) - T_n(x)), \tag{B 19}
$$

rather than $\hat{\psi}_{20}^{(2m)}$, to improve the numerical conditioning. The expansion (B 19) explicitly builds in the boundary conditions that $\mathrm{d}\hat{\psi}_{20}^{(2m)}/\mathrm{d}y$ vanishes at $y = 0$ and $y = y_{max}$ and, on application of the further condition that $\hat{\psi}_{20}^{(2m)}(y_{max}) = 0$, means that the expansion can be integrated to give

$$
\hat{\psi}_{20}^{(2m)} = \sum_{n=0}^{N} a_n \Theta_n(x)
$$
$$
\text{where } \Theta_n(x) := \begin{cases} \dfrac{4}{3} - \dfrac{3T_1(x)}{2} + \dfrac{T_3(x)}{6} & n = 0 \\[2mm] \dfrac{3}{8} - \dfrac{T_2(x)}{2} + \dfrac{T_4(x)}{8} & n = 1 \\[2mm] \dfrac{1 - T_{n+1}(x)}{n+1} + \dfrac{T_{n+3}(x) - 1}{2(n+3)} + \dfrac{T_{n-1}(x) - 1}{2(n-1)} & n \geqslant 2. \end{cases} \tag{B 20}
$$

Using $N = 100$ gives over 15 decades of drop off in $|a_n|$ and the solution is independent of y_{max} well before the actual value $y_{max} = 10$ chosen.

B.3. *Solvability condition at* $O(\delta^3/\epsilon^4)$

The problem for $\hat{\psi}_{30}^{(m)}$ is

$$
\left[\frac{\mathrm{d}^2}{\mathrm{d}y^2} - N_c\frac{\mathrm{d}}{\mathrm{d}y} - N_c(\hat{\sigma}_0 + 2\mathrm{i}y) \right]\frac{\mathrm{d}^2\hat{\psi}_{30}^{(m)}}{\mathrm{d}y^2} = -(J_0 + J_2) + \hat{\eta}_2\frac{\mathrm{d}^3\hat{\psi}_{10}^{(m)}}{\mathrm{d}y^3} + \hat{\sigma}_2\frac{\mathrm{d}^2\hat{\psi}_{10}^{(m)}}{\mathrm{d}y^2}, \tag{B 21}
$$

where the nonlinear terms are

$$
J_0 := \mathrm{i}[\hat{\psi}_{10}^{(m)} - \hat{\psi}_{10}^{(m)}(0)]\frac{\mathrm{d}^3\hat{\psi}_{20}^{(0)}}{\mathrm{d}y^3} - \mathrm{i}\frac{\mathrm{d}\hat{\psi}_{20}^{(0)}}{\mathrm{d}y}\frac{\mathrm{d}^2\hat{\psi}_{10}^{(m)}}{\mathrm{d}y^2} + \mathrm{c.c.}, \tag{B 22}
$$
$$
J_2 := \mathrm{i}\frac{\mathrm{d}\hat{\psi}_{20}^{(2m)}}{\mathrm{d}y}\frac{\mathrm{d}^2\hat{\psi}_{10}^{(m)*}}{\mathrm{d}y^2} + 2\mathrm{i}[\hat{\psi}_{20}^{(2m)} - \hat{\psi}_{20}^{(2m)}(0)]\frac{\mathrm{d}^3\hat{\psi}_{10}^{(m)*}}{\mathrm{d}y^3}
$$

$$-2\mathrm{i}\frac{\mathrm{d}\hat{\psi}_{10}^{(m)*}}{\mathrm{d}y}\frac{\mathrm{d}^2\hat{\psi}_{20}^{(2m)}}{\mathrm{d}y^2} - \mathrm{i}[\hat{\psi}_{10}^{(m)*} - \hat{\psi}_{10}^{(m)*}(0)]\frac{\mathrm{d}^3\hat{\psi}_{20}^{(2m)}}{\mathrm{d}y^3} + \text{c.c.}, \qquad (\text{B 23})$$

with boundary conditions that $\mathrm{d}\hat{\psi}_{30}^{(m)}/\mathrm{d}y(0) = 0$ together with $\hat{\psi}_{30}^{(m)}$, $\mathrm{d}\hat{\psi}_{30}^{(m)}/\mathrm{d}y$ and $\mathrm{d}^2\hat{\psi}_{30}^{(m)}/\mathrm{d}y^2$ all vanishing as $y \to \infty$. The operator on the left-hand side of (B 21) is non-self adjoint so we need to find the appropriate adjoint operator to develop a solvability condition. Defining the operator

$$\mathscr{L}_1 := \left[\frac{\mathrm{d}^2}{\mathrm{d}y^2} - N_c\frac{\mathrm{d}}{\mathrm{d}y} - N_c(\hat{\sigma}_0 + 2\mathrm{i}y)\right]\frac{\mathrm{d}}{\mathrm{d}y}, \qquad (\text{B 24})$$

then if $\Psi := \mathrm{d}\hat{\psi}_{30}^{(m)}/\mathrm{d}y$ (and subscripts indicate derivatives)

$$\int_0^\infty \Phi\mathscr{L}_1\Psi\,\mathrm{d}y = [\Phi\Psi_{yy} - \Phi_y\Psi_y + \Phi_{yy}\Psi + N(\Phi_y\Psi - \Phi\Psi_y) - N(\hat{\sigma}_0 + 2\mathrm{i}y)\Phi\Psi]_0^\infty$$
$$- \int_0^\infty \Psi\mathscr{L}_1^\dagger\Phi\,\mathrm{d}y, \qquad (\text{B 25})$$

where

$$\mathscr{L}_1^\dagger\Phi := -\frac{\mathrm{d}^3\Phi}{\mathrm{d}y^3} - N_c\frac{\mathrm{d}^2\Phi}{\mathrm{d}y^2} - N_c\frac{\mathrm{d}}{\mathrm{d}y}[(\hat{\sigma}_0 + 2\mathrm{i}y)\Phi]. \qquad (\text{B 26})$$

We need now to generate a solution $\hat{\Phi}$ of $\mathscr{L}_1^\dagger\Phi = 0$ such that all the boundary terms vanish. The required solution (unique up to arbitrary renormalisation) is, via variation of parameters,

$$\hat{\Phi} := \mathrm{e}^{-N_cy/2}\mathrm{Bi}[\zeta(y)]\int_0^y \mathrm{e}^{N_cx/2}\mathrm{Ai}[\zeta(x)]\,\mathrm{d}x - \mathrm{e}^{-N_cy/2}\mathrm{Ai}[\zeta(y)]\int_0^y \mathrm{e}^{N_cx/2}\mathrm{Bi}[\zeta(x)]\,\mathrm{d}x, \quad (\text{B 27})$$

where

$$\zeta(y) := \frac{N_c^{1/3}\hat{\sigma}_0}{(2\mathrm{i})^{2/3}} + \frac{N_c^{4/3}}{4(2\mathrm{i})^{2/3}} + (2\mathrm{i})^{1/3}N_c^{1/3}y. \qquad (\text{B 28})$$

This has $\hat{\Phi}(0) = \hat{\Phi}_y(0) = 0$ and $\hat{\Phi} \sim 1/y$ as $y \to \infty$, which ensures all the boundary terms in (B 25) vanish (recall $\Psi(0) = \mathrm{d}\psi_{30}^{(m)}/\mathrm{d}y(0) = 0$) and therefore means

$$\int_0^\infty \hat{\Phi}\mathscr{L}_1\frac{\mathrm{d}\hat{\psi}_{30}^{(m)}}{\mathrm{d}y}\,\mathrm{d}y = 0. \qquad (\text{B 29})$$

The solvability condition on (B 21) is then

$$I_1\hat{\sigma}_2 + I_2\hat{\eta}_2 = I_3 + I_4, \qquad (\text{B 30})$$

where

$$I_1 := \int_0^\infty \hat{\Phi}\frac{\mathrm{d}^2\hat{\psi}_{10}^{(m)}}{\mathrm{d}y^2}\,\mathrm{d}y, \quad I_2 := \int_0^\infty \hat{\Phi}\frac{\mathrm{d}^3\hat{\psi}_{10}^{(m)}}{\mathrm{d}y^3}\,\mathrm{d}y, \quad I_3 := \int_0^\infty \hat{\Phi}J_0\,\mathrm{d}y, \quad I_4 := \int_0^\infty \hat{\Phi}J_2\,\mathrm{d}y.$$
$$(\text{B 31}a-d)$$

Since the frequency shift $\hat{\sigma}_2$ is an imaginary number and the radial flow adjustment is real,

$$\hat{\eta}_2 = \frac{\text{Re}([I_3 + I_4]I_1^*)}{\text{Re}(I_2 I_1^*)} \approx 8.47 \times 10^4 > 0, \tag{B 32}$$

as computations give $I_1 = -24.17 - 75.26i$, $I_2 = 140.84 + 20.98i$, $I_3 = (3.262 + 4.1265i) \times 10^6$ and $I_4 = (2.949 - 0.5123i) \times 10^6$ (the contribution from the mean flow is an order of magnitude larger than that from the second harmonic, both in the same sense). So the bifurcation is supercritical with the bifurcating solution branch existing at radial flows larger than the critical value.

REFERENCES

ABRAMOWITZ, M. & STEGUN, I. 1964. *Handbook of Mathematical Functions*. Dover.
BAHL, S. K. 1970 Stability of viscous flow between two concentric rotating porous cylinders. *Def. Sci. J.* **20**, 89–96.
BALBUS, S. A. 2011 A turbulent matter. *Nature* **470**, 475–476.
CHANG, S. & SARTORY, W. K. 1967 Hydromagnetic stability of dissipative flow between rotating permeable cylinders. *J. Fluid Mech.* **27**, 65–79.
COUETTE, M. 1888 Sur un nouvel appareil pour l'etude du frottement des fluides. *Comptes Rendus* **107**, 388–390.
DEGUCHI, K., MATSUBARA, N. & NAGATA, M. 2014 Suction-shear-Coriolis instability in a flow between parallel plates. *J. Fluid Mech.* **760**, 212–242.
DOERING, C. R., SPIEGEL, E. A. & WORTHING, R. A. 2000 Energy dissipation in a shear layer with suction. *Phys. Fluids* **12**, 1955–1969.
DRAZIN, P. G. 1999 Flow through a diverging channel: instability and bifurcation. *Fluid Dyn. Res.* **24**, 321–327.
DRAZIN, P. G. & REID, W. H. 1981 *Hydrodynamics Stability*. Cambridge University Press.
DUBRULLE, B. 1992 A turbulent closure model for thin accretion disks. *Astron. Astrophys.* **266**, 592–604.
DUBRULLE, B., MARIE, L., NORMAND, C., RICHARD, D., HERSANT, F. & ZHAN, J.-P. 2005 A hydrodynamic shear instability in stratified disks. *Astron. Astrophys.* **429**, 1–13.
FARDIN, M. A., PERGE, C. & TABERLET, N. 2014 The hydrogen atom of fluid dynamics – introduction to the Taylor–Couette flow for soft matter scientists. *Soft Matt.* **10**, 3523–3535.
FARRELL, B. 1987 Developing disturbances in shear. *J. Atmos. Sci.* **44**, 2191–2199.
FRANK, J., KING, A. & RAINE, D. 2002 *Accretion Power in Astrophysics*, 3rd edn. Cambridge University Press.
FRANSSON, J. H. M. & ALFREDSSON, P. H. 2003 On the hydrodynamic stability of channel flow with crossflow. *Phys. Fluids* **15**, 436–441.
GALLET, B., DOERING, C. R. & SPIEGEL, E. A. 2010 Destabilising Taylor–Couette flow with suction. *Phys. Fluids* **22**, 034105.
GREENSPAN, H. P. 1968 *The Theory of Rotating Fluids*, p. 327. Cambridge University Press.
GUHA, A. & FRIGAARD, I. A. 2010 On the stability of plane Couette–Poiseuille flow with uniform crossflow. *J. Fluid Mech.* **656**, 417–447.
HAINS, F. D. 1971 Stability of plane Couette–Poiseuille flow with uniform crossflow. *Phys. Fluids* **14**, 1620–1623.
HOCKING, L. M. 1974 Non-linear instability of the asymptotic suction velocity profile. *Q. J. Mech. Appl. Maths* **28**, 341–353.
ILIN, K. & MORGULIS, A. 2013 Instability of an inviscid flow between porous cylinders with radial flow. *J. Fluid Mech.* **730**, 364–378.
ILIN, K. & MORGULIS, A. 2015a Instability of a two-dimensional viscous flow in an annulus with permeable walls to two-dimensional perturbations. *Phys. Fluids* **27**, 044107.

ILIN, K. & MORGULIS, A. 2015*b* Instability of an inviscid flow between rotating porous cylinders with radial flow to three-dimensional perturbations. arXiv:1502.02600v1.

JI, H. & BALBUS, S. A. 2013 Angular momentum transport in astrophysics and in the lab. *Phys. Today* **66**, 27–33.

JOSLIN, R. D. 1998 Aircraft laminar flow control. *Annu. Rev. Fluid Mech.* **30**, 1–29.

KERSALE, E., HUGHES, D. W., OGILVIE, G. I., TOBIAS, S. M. & WEISS, N. O. 2004 Global magentorotational instability with inflow. 1. Linear theory and the role of boundary conditions. *Astrophys. J.* **602**, 892–903.

KOLESOV, V. & SHAPAKIDZE, L. 1999 On oscillatory modes in viscous incompressible fluid flows between two counter-rotating permeable cylinders. In *Trends in Applications of Mathematics to Mechanics* (ed. G. Iooss, O. Gues & A. Nouri), pp. 221–227. Chapman and Hall/CRC.

KOLYSHKIN, A. A. & VAILLANCOURT, R. 1997 Convective instability of Couette flow between rotating porous cylinders with axial and radial flows. *Phys. Fluids* **9**, 910–918.

MALLOCK, A. 1888 Determination of the viscosity of water. *Proc. R. Soc. Lond.* A **45**, 126–132.

MARTINAND, D., SERRE, E. & LUEPTOW, R. M. 2009 Absolute and convective instability of cylindrical Couette flow with axial and radial flows. *Phys. Fluids* **21**, 104102.

MIN, K. & LUEPTOW, R. M. 1994 Hydrodynamic stability of viscous flow between rotating porous cylinders with radial flow. *Phys. Fluids* **6**, 144–151.

NICOUD, F. & ANGILELLA, J. R. 1997 Effects of uniform inhection at the wall on the stability of Couette-like flows. *Phys. Rev.* E **56**, 3000–3009.

OLVER, F. W. J., LOZIER, D. W., BOISVERT, R. F. & CLARK, C. W. (Eds) 2010 NIST handbook of mathematical functions. In *NIST Digital Library of Mathematical Functions*, Cambridge University Press; Release 1.0.9, online companion to http://dlmf.nist.gov/.

ORR, W. M. F. 1907 The stability or instability of the steady motions of a perfect liquid and of a viscous liquid. *Proc. R. Irish Acad.* A **27**, 9–138.

LORD RAYLEIGH 1880 On the stability, or instability, of certain fluid motions. *Proc. Lond. Math. Soc.* **11**, 57–70.

LORD RAYLEIGH 1917 On the dynamics of revolving fluids. *Proc. R. Soc. Lond.* A **93**, 148–154.

SERRE, E., SPRAGUE, M. A. & LUEPTOW, R. M. 2008 Stability of Taylor–Couette flow in a finite-length cavity with radial through flow. *Phys. Fluids* **20**, 034106.

SHARIFF, K. 2009 Fluid mechanics in disks around young stars. *Annu. Rev. Fluid Mech.* **41**, 283–315.

SQUIRES, H. B. 1933 On the stability for three-dimensional disturbances of viscous flow between parallel walls. *Proc. R. Soc. Lond.* A **142**, 621–628.

TAYLOR, G. I. 1923 Stability of a viscous liquid contained between two rotating cylinder. *Phil. Trans. R. Soc. Lond.* A **223**, 289–343.

TUCKERMAN, L. S. 2014 Taylor vortices versus Taylor columns. *J. Fluid Mech.* **750**, 1–4.